NOTICE

The quality of this microform is heavily dependent upon the quality of the original thesis submitted for microfilming. Every effort has been made to ensure the highest quality of reproduction possible.

If pages are missing, contact the university which granted the degree.

Some pages may have indistinct print especially if the original pages were typed with a poor typewriter ribbon or if the university sent us an inferior photocopy.

Previously copyrighted materials (journal articles, published tests, etc.) are not filmed.

Reproduction in full or in part of this microform is governed by the Canadian Copyright Act, R.S.C. 1970, c. C-30.

AVIS

La qualité de cette microforme dépend grandement de la qualité de la thèse soumise au microfilmage. Nous avons tout fait pour assurer une qualité supérieure de reproduction.

S'il manque des pages, veuillez communiquer avec l'université qui a conféré le grade.

La qualité d'impression de certaines pages peut laisser à désirer, surtout si les pages originales ont été dactylographiées à l'aide d'un ruban usé ou si l'université nous a fait parvenir une photocopie de qualité inférieure.

Les documents qui font déjà l'objet d'un droit d'auteur (articles de revue, tests publiés, etc.) ne sont pas microfilmés.

La reproduction, même partielle, de cette microforme est soumise à la Loi canadienne sur le droit d'auteur, SRC 1970, c. C-30.

Canada

Crystallographic Ordering in Chalcopyrite Semimagnetic Semiconductors

by

Daniel A. Bissonnette

Thesis submitted to the
School of Graduate Studies
in partial fulfillment of the requirements
for the degree of
Master of Science in Physics

Department of Physics
Faculty of Science and Engineering
University of Ottawa
Ottawa, Ontario

May 1988

ISBN 0-315-46719-3

UNIVERSITÉ D'OTTAWA
UNIVERSITY OF OTTAWA

Acknowledgements

I would like to express my thanks to Dr. John C. Woolley for his assistance and encouragement throughout the course of this work.

I would also like to thank Dr. G. Lamarche and Dr. A. Manoogian for the use of their labs and equipment.

Special thanks goes out to Bei Wah Chan for handling the ESR measurements.

I would like to thank Dr. Tom Holden and Dr. David Noakes for their assistance and expertise in the neutron diffraction measurements made at Chalk River.

As well I wish to thank Andrew Golebiowski, my Latex councellor, and Roger Goudreault, my graphics advisor, for their help in the formatting of this thesis.

Special thanks go out to my colleagues and good friends who made sports a compulsory course in the physics department.

Finally, a note of special gratitude goes out to my mother and father for their love and support throughout my graduate studies.

Abstract

During the present work, the thesis discusses an investigation into the possible crystallographic ordering arrangements that manganese can adopt within the chalcopyrite lattice of the separate pseudo binary alloy systems $(CuGa)_{1-z}Mn_{2z}Te_2$ and $(AgGa)_{1-z}Mn_{2z}Te_2$. These alloys belong to the class of materials known as semimagnetic semiconductors, an intermediate type which lies between non-magnetic and magnetic semiconductors.

Samples with different compositions from both systems were produced at the University of Ottawa by the melt and anneal technique. Debye-Scherrer x-ray photographs carried out during the present work along with previous optical energy gap and magnetic susceptibility measurements were used to accurately locate certain phase boundaries on the T(z) phase diagrams of the two systems. These determinations of the T(z) diagrams were made only after much of the present work had been completed. Samples were then used by a group at Merida to determine the phase diagram of both systems by the Differential Thermal Analysis (DTA) technique.

Magnetic susceptibility and Electron Spin Resonance (ESR) work was performed on various compositions of both systems. The presence of Mn-ordered and/or Mn-disordered phases could be detected from the temperature at which magnetic peaks in the susceptibility occurred and also by the value of the line widths in the ESR spectra. It was found from this work that metastable phases may occur within

a sample depending upon the type of heat treatment used. Samples of specific compositions of each system were therefore annealed at temperatures within the Mn-ordered chalcopyrite phase regions to allow the Mn-ordering process to take place.

Neutron diffraction measurements were carried out, in collaboration with Dr. Tom Holden and Dr. David Noakes at A. E. C. L. 's Chalk River Nuclear Labs, on specific compositions of each system in order to identify the type of Mn-ordering structure that was occurring. Preliminary calculations were carried out for proposed Mn-ordering arrangements where

a) the manganese enters only one of the cation sublattices at random and

b) all of the manganese enters at random the planes at height $\frac{c}{4}$ and $\frac{3c}{4}$ within the chalcopyrite lattice thus exhibiting a stannite-like structure.

These calculated intensities for the various types of reflections were then compared with the experimental diffraction spectra obtained in order to determine whether either ordered structures occurred. It was again found that these systems were very sensitive to the heat treatment a sample undergoes during the annealing and quenching periods. This was observed in the $(AgGa)_{1-z}Mn_{2z}Te_2$ system, where retention of high temperature phases during low temperature annealing periods had occurred.

The diffraction spectra showed that the $(CuGa)_{1-z}Mn_{2z}Te_2$ system probably doesn't have a Mn-ordered field in its equilibrium state as was shown later by its T(z) diagram. The $(AgGa)_{1-z}Mn_{2z}Te_2$ system's diffraction spectrum did not show

signs of either of the Mn-ordering types suggested above. This however could be due to the type of heat treatment used in this case. However, the $(AgGa)_{1-z}Mn_{2z}Te_2$ sample did exhibit an interesting behavior that can be attributed to another type of ordering in which the manganese totally fills a limited number of planes in the chalcopyrite lattice that are perpendicular to the c axis (planar-type Mn-ordering).

Contents

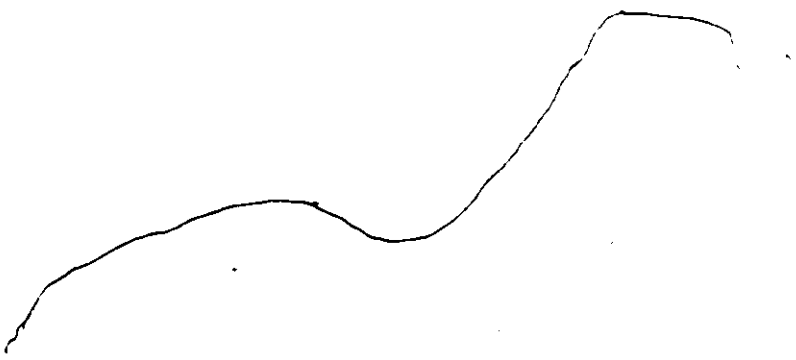

List of Figures

Chapter 1

Introduction

1.1 General Introduction

In recent years, there has been considerable interest in a group of alloys which form an intermediate class of materials between non-magnetic and magnetic semiconductors. They are widely known as either diluted magnetic semiconductors, (DMS), or semimagnetic semiconductors, (SMSC) .

These types of materials are obtained by alloying an ordinary semiconductor with a magnetic semiconductor. The presence of paramagnetic ions in the host semiconductor causes differences in the semiconductor's properties [3,9,11]. Some of these property changes include:

1- giant magneto-optical effects,

2- enhanced Zeeman splitting of the bands,

3- magnetic field dependence of the acceptor activation energy,

4- a spin glass behavior,

and other unique electrical and optical effects contained in the text and references of several review articles which will not be dealt with in this report.

1.2 Crystallography

1.2.1 Adamantine Materials

Any material with a crystallographic structure derived from the tetrahedrally bonded diamond structure can be called adamantine. Typical examples of these are the Group IV elements which crystallize in the diamond structure, the II-VI compounds which have the zinc-blende structure and various ternary compounds which crystallize in the chalcopyrite lattice structure. These structures are adamantine if they fulfill two basic requirements:

1. There must be an average of four valence electrons per lattice site.

2. There must be an equal number of anion and cation sites.

It is possible to produce alloys using the $MnTe$ and chalcopyrite $I\text{-}III\text{-}VI_2$ compounds which satisfy these conditions. Since these latter materials are the ternary analogs to the II-VI compounds, they are expected to have very similar crystal structure.

1.2.2 The zinc-blende and chalcopyrite structures

The zinc-blende lattice structure of the II-VI materials is derived from the tetrahedrally bonded diamond structure in such a way that one of the fcc sublattices

is occupied by the cation (II), while the anions (VI) are positioned on the other sublattice, giving an average of four valence electrons per lattice site. The structure of the zinc-blende lattice and a projection of the atomic positions are depicted in Figure 1. The Group II atoms are tetrahedrally bonded to the Group VI atoms that are displaced by a/4 along the face diagonal. The symmetry of the zinc-blende lattice is reduced from that of the diamond lattice because of the ordering of the two different types of atoms. If all the atoms in Figure 1 were identical, the diamond structure would be obtained.

The compounds and alloys formed from the combination of Groups I, III and VI atoms are also adamantine and have a $CuFeS_2$ chalcopyrite lattice structure. Due to the ordering of the two types of cations (I and III) on two different sublattices along with one anion sublattice (Figure 2), the unit cell is no longer cubic. In this structure atoms of Group I and III are tetrahedrally coordinated by four Group VI atoms; where each of the Group VI atoms is in turn coordinated by two atoms of each of the I and III Group. These materials have a body centered tetragonal lattice with the c/a ratio equal to or less than 2, with its unit cell containing 16 atoms.

1.3 Manganese Ordering on the Zinc-Blende and Chalcopyrite Crystallographic Lattice

Previous measurements performed on different types of these SMSC made by other members of our research group at the University of Ottawa [24] showed that, despite the apparent single phase condition of the x-ray photographs, two different magnetic

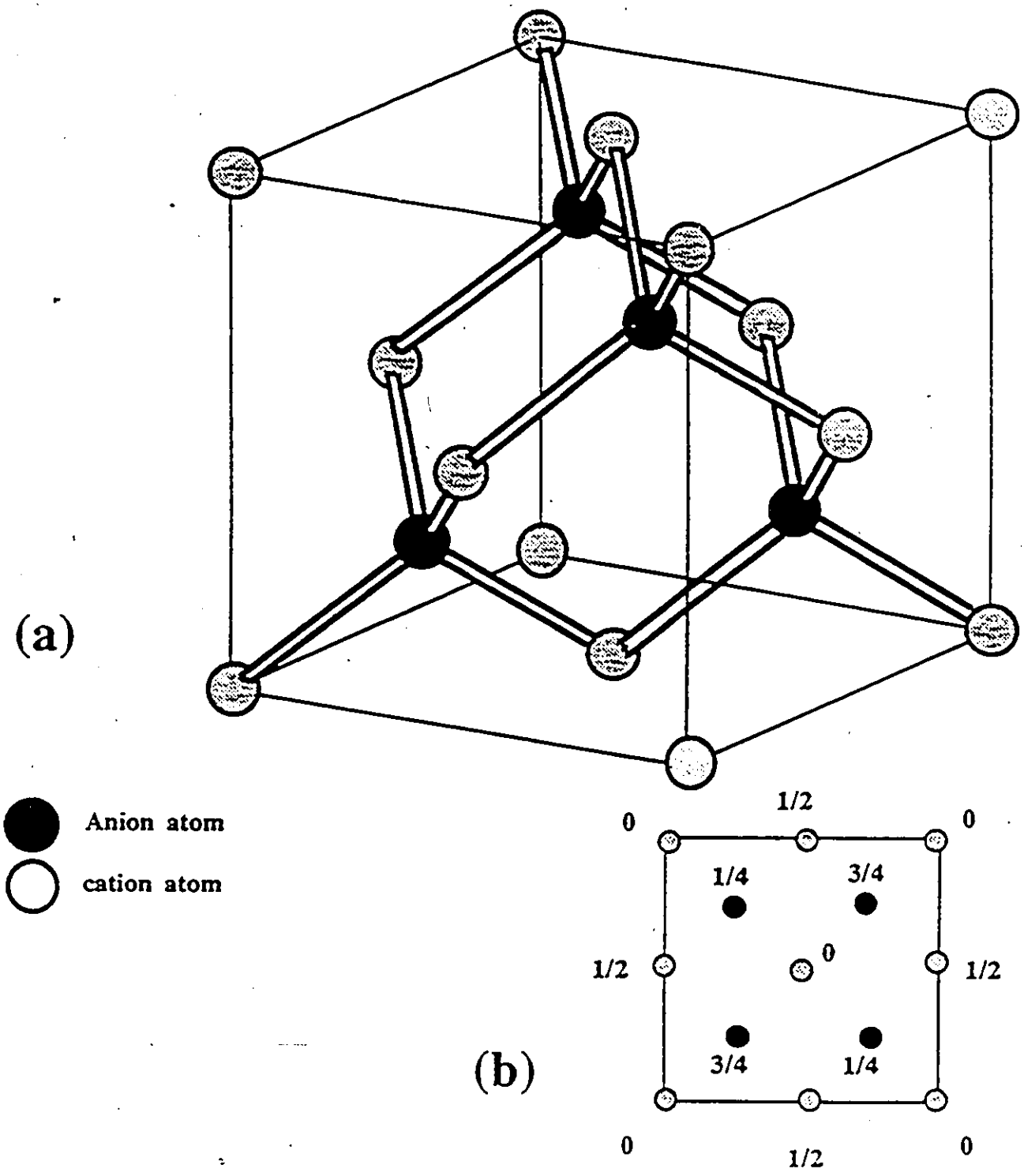

Figure 1: (a) Zinc-Blende structure with (b) projection of atomic positions on the c face

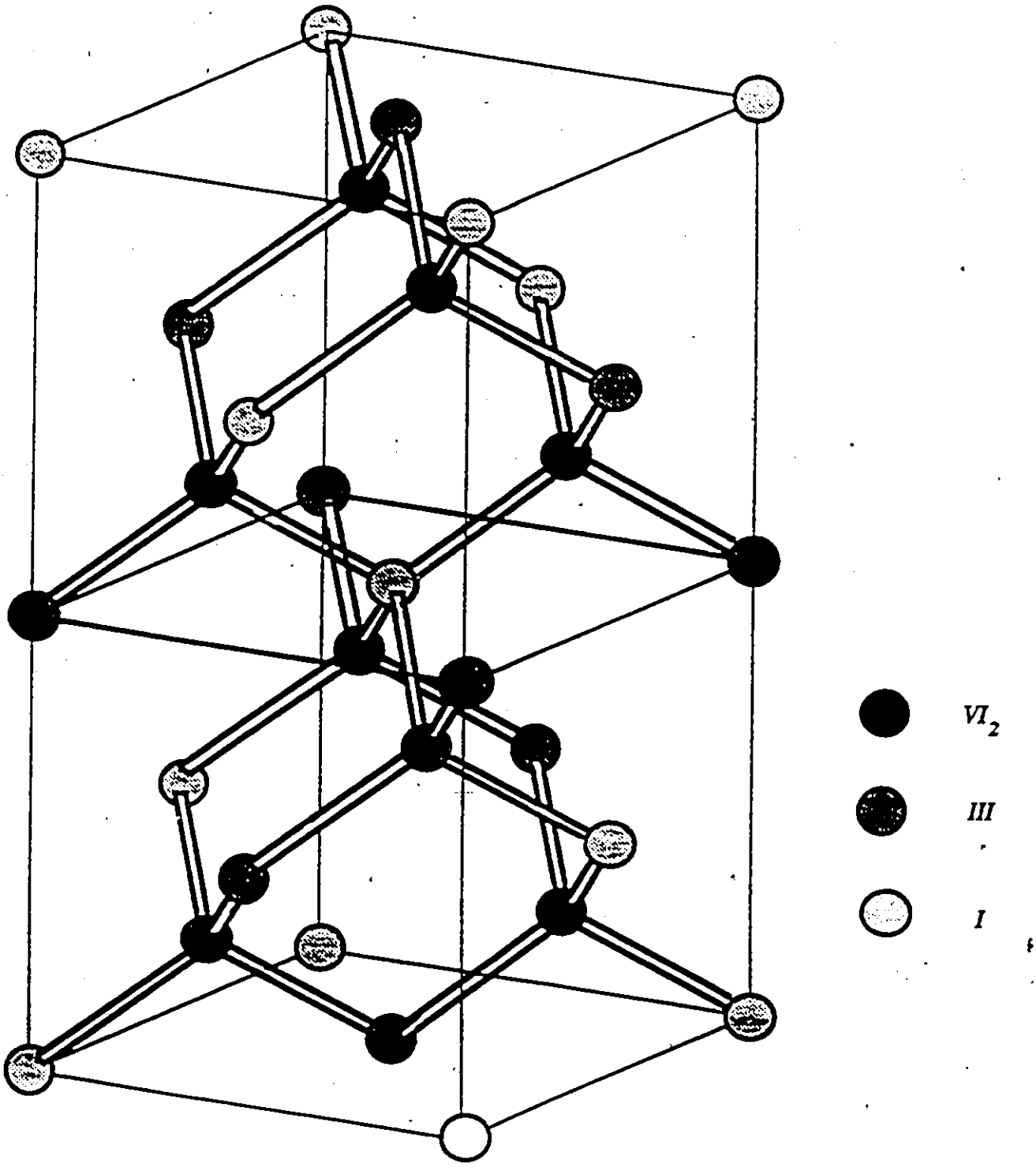

Figure 2: Chalcopyrite lattice

phases were observed. These are attributed to crystallographic ordering of the manganese atoms. The lattice parameter values determined from x-ray photographs for both zinc-blende and chalcopyrite in no way show any change of lattice parameter as the Mn-disordered phase becomes Mn-ordered. The lattice parameters slowly increase as the manganese concentration is increased, as is normally expected from these materials.

In the present work, further measurements on the $(AgGa)_{1-z}Mn_{2z}Te_2$ and $(CuGa)_{1-z}Mn_{2z}Te_2$ systems were made at the University of Ottawa and, in collaboration with Dr. Tom Holden and Dr. David Noakes of the Neutron Physics branch at A. E. C. L. 's Chalk River Nuclear Laboratories, neutron diffraction measurements were taken to identify the Mn-ordered structure. The indication of this order-disorder transition appearing in the experimental measurements will be discussed below.

1.3.1 Mn Order-Disorder in Magnetic Susceptibility

From magnetic susceptibility measurements made in the present work and by other members of the group on these materials [1,12,16] two peaks were usually observed in the susceptibility versus temperature curve. The lower temperature peak in the measurement corresponds to the Mn-disordered structure in which the magnetic ions are randomly distributed on the lattice site and the higher transition temperature corresponding to the antiferromagnetic ordering of the magnetic ions in the structure. A plot of the variation of each transition temperature as a function of manganese concentration shows two separate straight lines for both the chalcopyrite and zinc-blende cases [24]. The relative size of a peak observed in the magnetic

susceptibility curve is a result of the amount of phase present. By extrapolating the ordered and disordered lines down to lower temperatures, we see that the lines corresponding to the zinc-blende structure extrapolate to an experimental percolation limit. This experimental percolation limit agrees with the theoretical percolation limit calculated for the zinc-blende structure.

The variation of θ, the Curie-Weiss paramagnetic temperature, with manganese concentration was also plotted. However, the value of θ was the weighted average of those for the ordered and disordered phases and thus the values obtained lie between two theoretically predicted limits. The upper limit corresponds to the crystallographic ordering of the manganese and the lower limit to the completely random manganese distribution. However, it is important to mention that in the case of a few samples, the values of θ were found to confirm the calculated value for either one phase or the other. This depends on the degree of manganese order and disorder existing in the sample.

1.3.2 Mn Order-Disorder in Optical Energy Gap

In measurements of energy gap, E_o, made on different alloy systems by members of the research group [1,12] each magnetic phase present in each structure (zinc-blende and chalcopyrite) showed remarkably different energy gap values. When a diagram of E_o versus manganese concentration is plotted for say zinc-blende, we obtain a straight line that drastically changes direction at some point. This sudden change in slope is attributed to the phase change occuring between the disordered and ordered structure. When all these lines are extrapolated to manganese concentration $x = 1$, all lines give different energy gap values. These values represent the energy gaps

that MnTe would have if it would crystallize in the ordered and/or disordered chalcopyrite and/or zinc-blende structures. For all the different systems that were analyzed [24], all the extrapolated lines give intercepts (or theoretical MnTe energy gap values) that were consistent for the appropriate structure. The intercepts were as follows:

Mn-Ordered Zinc-Blende: 1.9 eV

Mn-Disordered Zinc-Blende: 2.85 eV

Mn-Ordered Chalcopyrite: 1.35 eV

Mn-Disordered Chalcopyrite: insufficient data

It was found that the energy gap of these samples depend on whether the magnetic ions in the samples are ordered or disordered within the lattice. This is described in more detail by Woolley et al. [24].

1.3.3 Mn Order-Disorder in ESR

From the ESR measurements made by other members of the group [1,12] and in the present work, two absorption lines were usually observed in each of the chalcopyrite and zinc-blende cases. The presence of two lines in the ESR spectrum verify the results obtained in the susceptibility and the optical energy gap measurements which indicated the presence of two different magnetic phases. The narrow sharp absorption line was attributed to the presence of the ordered phase and the broader line to the presence of the disordered phase.

Further experimental measurements are being made to determine the ordered structure of various SMSC [4].

1.4 Investigation of the Mn-Ordered Structure

Now that the presence of two different magnetic phases (Mn-ordered and Mn-disordered) in different SMSC has been established, a more detailed investigation of the ordered structure has been underway. This work will mainly deal with the investigation and possible determination of the ordered structure within the chalcopyrite compositional range of the alloys of both $CuGaTe_2$ and $AgGaTe_2$ systems respectively, with $MnTe$, through;

I - further magnetic susceptibility, ESR and x-ray diffraction measurements performed at the University of Ottawa,

II - investigation of the phase diagrams of both systems by Differential Thermal Analysis measurements made primarily at Merida [18] on samples all prepared at the University of Ottawa during this work (a similar DTA apparatus was constructed at the University of Ottawa but was not ready for measurements in time for the work in this thesis),

III - neutron diffraction measurements carried out, in collaboration with Dr. Tom Holden and Dr. David Noakes at the Chalk River Nuclear Labs, on specific alloy compositions of both systems with $MnTe$.

In the present thesis, results and data from the other members of the group at the University of Ottawa will be quoted and used to complement and verify some results of the present work. In all such cases, appropriate references will be made.

The present work deals mainly with the determination of the Mn-ordered structure in the chalcopyrite compounds by methodical analysis and comparison with

proposed Mn-ordered structures. The determination of the actual ordered structure of these SMSC systems will help broaden our understanding of their properties, especially those involving magnetic exchange interactions.

Chapter 2

Preparation of Samples and Phase Diagrams

2.1 Introduction

Lattice parameter, optical energy gap and magnetic measurement data on the $(AgGa)_{1-z}Mn_{2z}Te_2$ system has been previously collected and analysed by Munkid Al Najjar [1]. The same measurements were performed by Roger Goudreault [12] on the $(CuGa)_{1-z}Mn_{2z}Te_2$ system. Magnetic measurements were also made on various $(I-III)_{1-z}Mn_{2z}Te_2$ alloys by other members of the group [15,16]. In the present work, further measurements were made on the two former alloy systems concentrating more on the chalcopyrite alloys of both systems.

The previous results [24] indicated that ordering of the manganese ions on the cation sublattice occurs in these alloys and that this has a significant effect on the magnetic behavior and on the optical energy gap values. To examine these effects

in more detail it is necessary to have information concerning the phase diagram and the ordered structure of these alloys.

For the purpose of this work, samples of both alloys were prepared and annealed at the University of Ottawa. The annealing temperature to be used in any given case was uncertain until the T(z) phase diagram had been determined. The DTA measurements performed by a group at Merida [18] showed the presence, in the $(AgGa)_{1-x}Mn_{2x}Te_2$ case, of the manganese ordered and disordered phases as had been indicated from ESR, magnetic susceptibility and optical energy gap results.

Specific compositions of these alloys were annealed within the Mn-ordered temperature region to encourage the ordering process. A fairly lengthy annealing time was used after which each sample was rapidly quenched to trap into the structure as much of this Mn-ordered phase as possible.

The quenched samples were then checked for reasonable equilibrium conditions using the Debye-Scherrer x-ray diffraction method. They were also scrutinized thru ESR (Electron Spin Resonance) measurements for the presence of the Mn-ordered phase. It was found that lattice parameter values obtained further clarified the T(z) phase diagram of each system. As will be discussed later, neutron diffraction measurements were then performed on the appropriate samples to identify the Mn-ordered structures involved.

2.2 Preparation of Samples

To investigate the properties of interest of various alloys, about thirty samples of different compositions were made using the melt and anneal technique.

The constituent elements were sealed under vacuum in quartz tubes. The lengths of the sealed tubes were generally between four and five cm. A total of nine grams of each sample was found to be needed for the various types of measurements to be made since the neutron diffraction study would require at least six grams of material.

To avert having the quartz tubes crack during the melting and subsequent cooling processes because of excessively large amount of materials present, a set of three samples of approximately three grams each was made for each specific alloy composition. The three samples in each set would later be combined after the annealing phase to become one big nine gram sample.

To prevent some of the elements, particularly manganese, from reacting with the quartz during the melting process, the interior of the tubes were carbonized in the following manner. After one end of an ampoule had been sealed, a piece of acetone soaked absorbent paper was placed in the open end of the ampoule. The sealed end was heated over an open flame. A layer of carbon would deposit at the hot end of the tube as soon as the acetone vapour concentration was high enough. The heating process was continued until the carbon layer was thick enough to be opaque under a strong light source. Afterward, each tube was flushed with acetone to remove any foreign material that could have entered.

Having been carbonized, flushed and filled with the appropriate weight of each element required, the tubes were then sealed under a vacuum of about 10^{-5} mm Hg. The melting temperatures of the various elements which make up these systems are listed in Table 1. These high melting points approached the highest temperature which could be attained by the melting furnace. Consequently, the samples would

Element	Melting Point (^0C)
Cu	1083
Ga	29.78
Ag	960.8
In	156.4
Mn	1240
Te	449.5

Table 1: Melting Temperature of Elements

have to be held at this highest temperature for a period of time to allow any portion which had not melted to be completely dissolved.

Therefore the ampoules were placed in the melting furnace and heated to about 1200^{0}C and kept at this temperature for about 1 1/2 hours. During this process the tubes were shaken periodically to ensure proper mixing of the contents. The furnace was then switched off with the samples left to cool to room temperature inside it. Considering the size of the samples, this procedure helped avoid breakage of the quartz upon solidification of the alloy.

The samples were then annealed so as to make them into a homogeneous material because of the possible segregation of elements and phases on cooling from the melting process. A better homogeneity within a single phase region could be induced if the annealing temperature was high enough and the annealing period long enough to facilitate the diffusion of the components within the samples.

It was found that because the samples were in the form of solid ingots, very long annealing times were necessary to attain an equilibrium condition. As had been found previously for other alloys [23], equilibrium was reached much more quickly if the sample was powdered after melting and the powder then compressed and annealed. Thus, all samples were made and then annealed in the compressed

powder form.

The samples were annealed at about 600°C for 4-5 weeks then they were taken out and cooled in air. As they slowly cooled, the alloys were able to retain a fairly good equilibrium state right down to room temperature. It was found through X-ray powder photographs that this particular choice of annealing time and temperature produced reasonably good equilibrium and homogeneity conditions in all the samples.

About 50-100 mg specimens for a range of sample compositions were extracted from each ingot and used in DTA (Differential Thermal Analysis) measurements, as will be discussed in Section 2. 3.

After good equilibrium had been reached during the initial annealing period, as confirmed by good resolution of the high angle lines in the x-ray photographs, all the samples were re-annealed at different temperatures. These annealing periods were done at different temperatures to help find lattice parameter values and to accurately locate vertical phase boundaries in the subsequent T(z) phase diagrams.

From the T(z) phase diagrams obtained and the other measurements performed indicating the presence of Mn-ordered structures, the samples were reannealed at the appropriate ordering temperatures to promote the short range diffusion within each lattice. These new structures were expected to be zinc-blende and/or chalcopyrite with the manganese ions ordered and/or disordered on the appropriate sublattices.

2.2.1 X-Ray Analysis

To determine lattice parameter values and solid solution limits for the zinc-blende and/or chalcopyrite structures present, room temperature Debye-Scherrer x-ray diffraction photographs were taken using CuK_α radiation. This powder method consists of grinding a specimen to a fine powder and applying it to a glass holder with grease. The holder is put into a camera and then rotated automatically while immersed in a CuK_α radiation beam for 3 to 6 hours. After exposure, the lattice parameters can be determined by measuring the positions of the diffracted lines on the film and finding the corresponding Bragg angles.

It is known that the angles so obtained are not always the correct Bragg angles since various effects such as shrinkage of the film, absorption in the specimen, etc. can displace the diffraction lines from the true positions. Two methods have been used to eliminate these effects. They are the Nelson-Riley extrapolation method and the internal calibration technique. These methods will be discussed later.

Analysis for the Cubic Zinc-Blende Structure

Once you index the cubic powder pattern, the lattice parameter a can be determined by using the Bragg condition for diffraction for the cubic case which is given by the expression:

$$\sin^2\theta = \frac{\lambda^2 N}{4a^2} \tag{1}$$

where θ is the Bragg angle,

λ is the incident beam wavelength,

$N = h^2 + k^2 + l^2$ is an integer

where h, k and l are the Miller indices

of each scattering plane

and a is the lattice parameter.

For a simple cubic lattice, any possible set of (hkl) values can occur. For fcc lattices, only certain N values are allowed. For diffraction maxima to occur in a fcc lattice, the h, k and l values have to be all even or all odd. Also, for the zinc-blende case, the indices satisfy the conditions:

$$\begin{aligned} h+k+l &= 4n \qquad I \propto (F_{hkl})^2 = 16(f_A + f_B)^2 \\ h+k+l &= 4n+2 \qquad I \propto (F_{hkl})^2 = 16(f_A - f_B)^2 \\ h+k+l &= 2n+1 \qquad I \propto (F_{hkl})^2 = 16(f_A^2 + f_B^2) \end{aligned} \tag{2}$$

where f_A and f_B are the atomic scattering factors and F_{hkl} is the structure factor of individual scattering planes and its square is proportional to the intensity of the line.

Therefore, individual lines have differing intensities according to their Miller indices and multiplicity factors. For zinc-blende, we can see strong reflection occuring at N= 3, 11, 16, 19, etc. and weak reflection occurs at N= 4, 12, 20, etc. With the proper labelling of (hkl) Miller indices and subsequent Bragg angle determination for the lines, the approximate lattice parameter values for the lines can be identified. To find the true lattice parameter, we apply the Nelson-Riley extrapolation method. In this method, the lattice parameter for each Bragg angle is plotted as a

function of the semi-empirical function $f(\theta)$ where:

$$f(\theta) = \frac{1}{2}\left(\frac{\cos^2\theta}{\sin\theta} + \frac{\cos^2\theta}{\theta}\right) \tag{3}$$

This function, $f(\theta)$, corrects for the absorption due to the finite dimensions of the specimen on the holder. The true lattice parameter is obtained by extrapolating to $f(\theta) = 0$ on the lattice parameter axis. For high precision, the high angle lines must be used and the lines must be sharp with the K_α doublet well resolved.

Analysis for the Chalcopyrite Structure

For chalcopyrite materials, which have the tetragonal symmetry, the Bragg condition is given by:

$$\sin^2\theta = \frac{\lambda^2}{4}\left(\frac{h^2 + k^2}{a^2} + \frac{l_T^2}{c_T^2}\right) \tag{4}$$

where θ is the Bragg angle,

λ is the incident beam wavelength,

h, k and l_T are chalcopyrite Miller indices

and a and c_T are lattice parameters.

The zinc-blende and chalcopyrite structures have the same atomic positions when $c/a = 2$. Therefore all diffraction lines of the zinc-blende structure will occur in the cnalcopyrite structure. In addition to the zinc-blende lines, the chalcopyrite structure will also have a set of ordering lines occuring.

This can be explained in the following manner. If both structures exhibit the same values of $\sin^2\theta$ when $c_T = 2c_{ZB}$ then we must have that $l_T = 2l_{ZB}$. Therefore,

Zinc-Blende		Chalcopyrite
N	(hkl)	(hkl)
1.25	—	(101)
3	(111)	(112)
3.25	—	(103)
4	(200)	(200), (004)
5.25	—	(211)
7.25	—	(213), (105)
8	(220)	(220), (204)
9.25	—	(301)
11	(311)	(312), (116)
11.25	—	(303), (215)
12	(222)	(224)
13.25	—	(321), (107)
15.25	—	(323), (305)
16	(400)	(400), (008)
17.25	—	(411), (217)
19	(331)	(332), (316)
19.25	—	(413), (325)
20	(420)	(420), (404), (208)
21.25	—	(307), (109)
23.25	—	(415)
24	(422)	(424), (228)
25.25	—	(501), (431), (327), (219)
27	(333), (511)	(336), (512), (1110)
27.25	—	(503), (433)
29.25	—	(521), (417), (309)

Table 2: Low angle Miller indices for zinc-blende and chalcopyrite structures.

all lines labelled hkl_{ZB} in zinc-blende will be labelled $hk2l_{ZB}$ for the chalcopyrite case. For example, with $N = 20$, the Miller index in the zinc-blende case is (420) and that in the chalcopyrite case is (420), (404) and (208), because the index l_{ZB} of the zinc-blende can be 4, 2 and 0 respectively. When the chalcopyrite ratio $c/a = 2$, the (420), (404) and (208) diffraction lines would occur at exactly the same Bragg angle θ. For the case where $c/a \neq 2$, these diffraction lines split showing three separate lines.

If we apply this analysis to the chalcopyrite ordering lines, we see that half integral l_{ZB} values are obtained indicating that the l_T value is odd. For example, if a chalcopyrite ordering line has a value of $N = 1.25$ on the basis of a zinc-blende analysis, then it must have hkl_{ZB} values of $(1,0,\frac{1}{2})$. By doubling the l_{ZB} value, the corresponding (h,k,l_T)values for the chalcopyrite structure are (1,0,1). Table 2 illustrates the low Bragg angle combinations of (hkl) values for zinc-blende and chalcopyrite structures.

Having determined θ, the Bragg angle, from the x-ray film and having labelled each line with the proper Miller index, the approximate parameters a and c can be found.

Another method to determine accurate lattice parameters is the internal calibration method. In this method, an internal standard sample with an accurately known parameter is mixed with the sample being investigated. The value of the Bragg angle for both materials can then be calculated from the film. A correction curve of $\Delta \sin^2\theta$ versus $\sin^2\theta$, to allow for absorption effects etc. , is calculated from the data for the standard material. Hence, the corrected values of $\sin^2\theta$ for the unknown sample are obtained. Accurate lattice parameters of the sample being

investigated are then obtained.

In the present work, the samples with cubic zinc-blende structure had their lattice parameters accurately measured using the Nelson-Riley method. Because of the difficulty involved with this method in determining two accurate lattice parameter values in a tetragonal system where $c/a \neq 2$, the internal calibration method was used with such chalcopyrite structured samples.

2.3 Phase Diagrams

2.3.1 Differential Thermal Analysis Technique

Differential Thermal Analysis (DTA) is a technique for studying the thermal transitions that a substance undergoes upon heating and cooling. It makes use of the fact that structural changes are accompanied by evolution or absorption of heat. It is merely a measure of a substance's energy content as a function of temperature.

This method requires one to place a sample in a furnace, which has a predetermined temperature variation capability, and measure the temperature difference, ΔT, between the sample under investigation and a reference standard as a function of temperature. The deviation of ΔT from its near zero value on the resulting thermograms indicate the temperature at which transitions and changes in state occur.

Although the DTA analysis is a relatively simple technique it is important to realize that in systems which prove difficult to achieve equilibrium, this thermal method of analysis must be treated with caution because "true" equilibrium may not be attained at each temperature. One can verify the equilibrium state of a

sample by annealing it at high temperatures in the sub-solidus region for varying lengths of time. If each DTA analysis for each different annealing time gives identical thermograms then the sample has reached a "metastable" equilibrium. Also, this method is apt to be unclear when determining steep falling solidus or liquidus curves. For these reasons, it is usually necessary to corroborate thermal analysis studies with x-rays of specimens quenched from solidus temperatures in order to confirm the composition of the crystalline phases.

A DTA apparatus was designed and built in Merida and used to investigate the $T(z)$ diagrams of the $(AgGa)_{1-z}Mn_{2z}Te_2$ and $(CuGa)_{1-z}Mn_{2z}Te_2$ systems from room temperature up to 1000°C. A similar apparatus was built at the University of Ottawa but was not available for measurements while the present work was being carried out.

In this apparatus, a 50 mg Ag standard and a 50 mg sample are contained in evacuated quartz ampoules having re-entrant thermocouple wells at the bottom. The ampoules are placed in a quartz holder that supports two chromel-alumel thermocouples and one differential chromel-alumel thermocouple. The differential thermocouple has two junctions one placed in each of the standard and sample thermocouple wells. The other regular thermocouples are in close proximity to the samples, one used for direct temperature reading and the other for control of heating system.

Heating is accomplished using an aluminum encased vertical resistance furnace controlled by a saturable core reactor. With this heating arrangement, the samples were heated at a rate of about 15°C/min. and then cooled at an average rate of 4°C/min.

The thermograms are obtained by the conventional technique of plotting the difference in temperature, ΔT, between the sample and standard on a two pen y-t recorder (Hewlett-Packard), versus time. A profile of the sample temperature versus time is simultaneously obtained to give the temperature at which phase changes occur.

2.3.2 Phase and Crystallographic Results

DTA measurements were made by a group at Merida, [18], for a compositional range of the $(CuGa)_{1-z}Mn_{2z}Te_2$ and $(AgGa)_{1-z}Mn_{2z}Te_2$ systems. The samples used were all prepared in Ottawa during this work and the measurements were made after much of the preparation work had been completed. 50-100 mg specimens were used that had all been prepared at the University of Ottawa during the present work. Since the work in question was to investigate SMSC alloys, the compositional range of each system was limited to $0 \leq z \leq 0.7$ and the behavior of the Mn-rich phase was not considered. Therefore, a maximum temperature of 1000^0C was sufficient for the work with silver used as the reference material. Each sample investigated was subjected to heating and cooling runs in the process.

The results of the DTA measurements for both systems are shown by the points in Figures 3 and 4 where heating and cooling curve data are indicated separately. The proposed phase boundaries that were obtained using these points are shown as full lines and the phase boundaries estimated from the x-ray and energy gap results are shown as dotted lines. In the present work, the phases shown in both diagrams are;

α: chalcopyrite phase

β: zinc-blende phase

γ: hexagonal NiAs structure of MnTe

η: Cu_2Te-rich hexagonal phase

δ: rock salt structure (high temp. MnTe)

In the case of the chalcopyrite (α) and zinc-blende (β) single phase fields, results indicate that ordering of the manganese can occur at lower temperatures to give ordered α' and β' structures. This manganese ordering has an appreciable effect on the energy gap E_o. The two T(z) diagrams will be discussed separately in the following sections.

$(CuGa)_{1-z}Mn_{2z}Te_2$ Phase Diagram

The proposed phase diagram of the $(CuGa)_{1-z}Mn_{2z}Te_2$ alloy system is shown in Figure 3. It was drawn combining the results of DTA and x-ray investigations carried out on different samples with a step in z of 0.05 near the terminal points and of 0.10 for the rest. The x-ray investigations were performed by members of both groups.

It was not possible to obtain the phase boundary between the α and $(\alpha+\gamma)$ fields from DTA data. Thus, samples were annealed at different temperatures and then quenched rapidly to retain as much of the equilibrium condition at the annealing temperature. Afterwards, structure and lattice parameters were determined by x-ray photographs and the values of a as a function of z for both chalcopyrite and zinc-blende were found as shown by Figure 5.

Small samples were annealed at 600°C and 650°C and then quenched rapidly

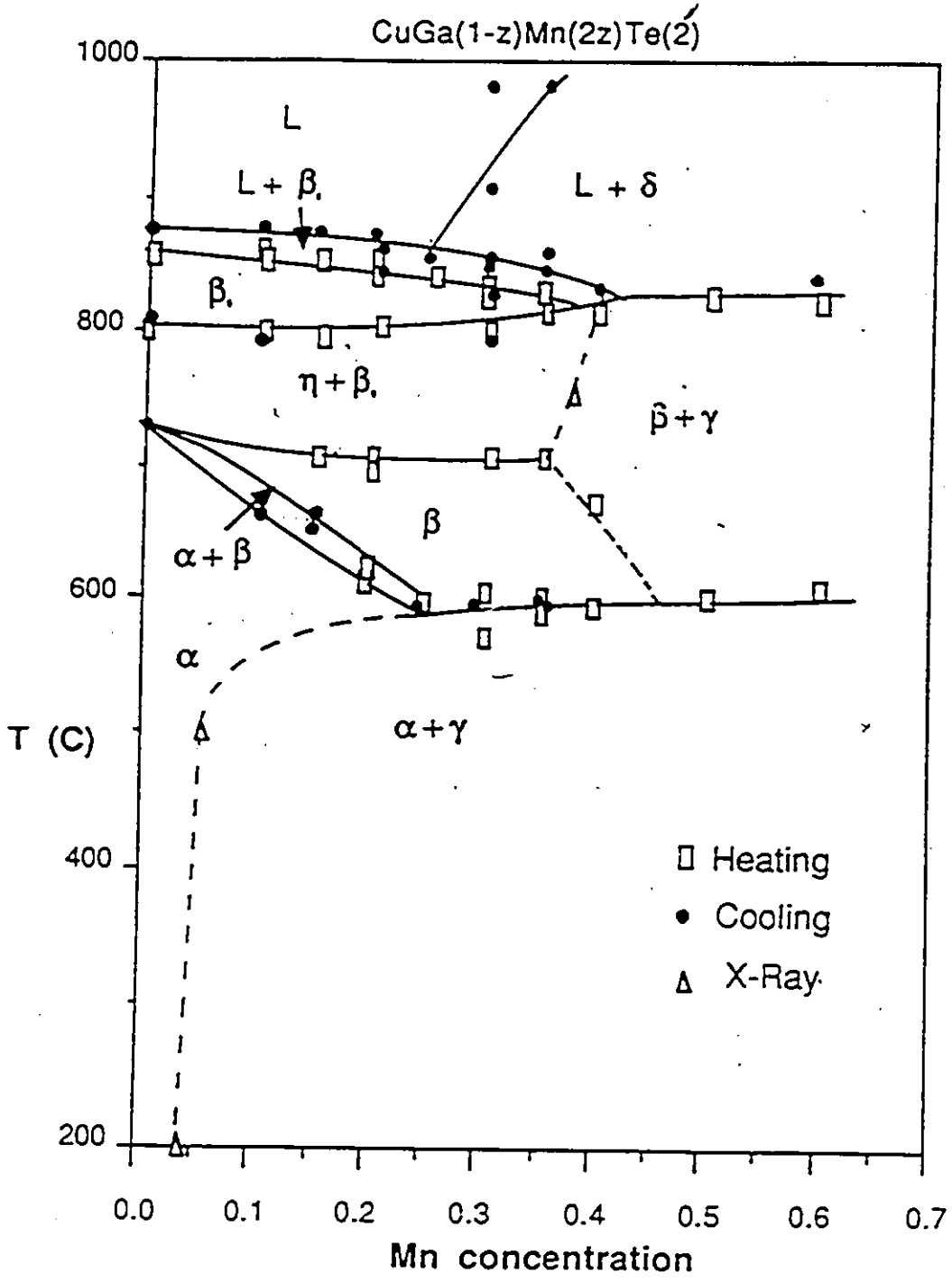

Figure 3: T(z) diagram for $(CuGa)_{1-z}Mn_{2z}Te_2$ alloys

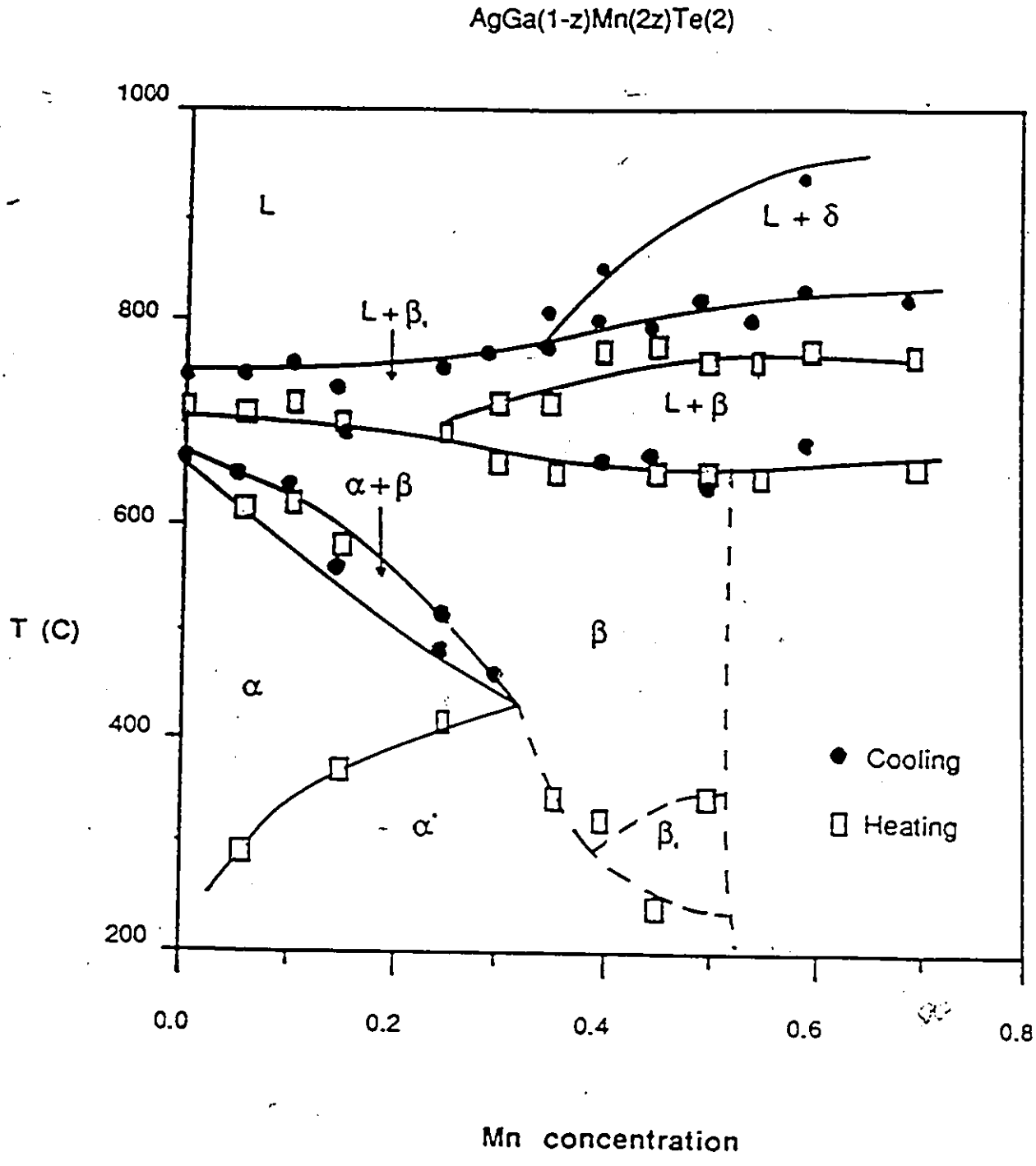

Figure 4: T(z) diagram for $(AgGa)_{1-z}Mn_{2z}Te_2$ alloys.

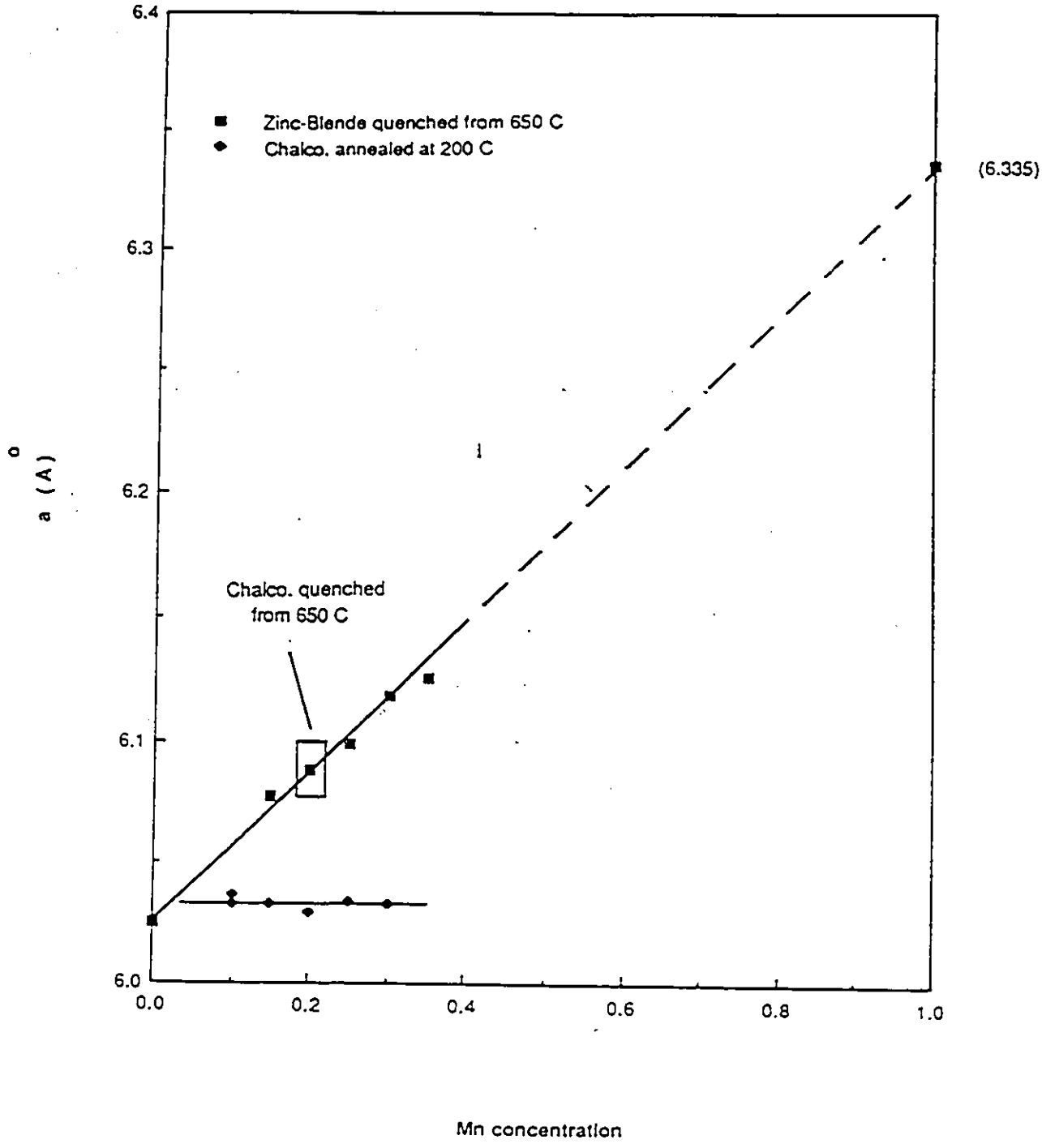

Figure 5: Variation of lattice parameter a with concentration z for $(CuGa)_{1-z}Mn_{2z}Te_2$ alloys.

in water to check the high temperature part of the phase diagram. Many samples were found to be a mixture of the phases occuring in the cooling process and appeared to depend critically on the cooling conditions. However, obtaining lattice parameter values, magnetic transition temperatures, etc. for a particular phase was often possible.

As can be seen in Figures 5 and 6, all the samples which had been slowly cooled to 200°C were found to be two phase ($\alpha + \gamma$). The lattice parameter and energy gap values of the chalcopyrite contribution to both phases showed that the tie lines in this field probably lie in the plane of the diagram.

Samples with composition $z = 0.10$ and $z = 0.15$ were annealed at 600°C and quenched rapidly in an attempt to get the chalcopyrite single phase. Both phases, ($\alpha + \gamma$), were still observed although faint lines of the single phase α condition at 600°C were seen in the $z = 0.15$ sample and its approximate a value calculated as is shown in Figure 5.

Various other samples, $z = 0.2$, $z = 0.25$, $z = 0.30$ and $z = 0.35$, were annealed at 650°C and then quenched to retain the single phase β. The $z = 0.30$ and $z = 0.35$ showed the single phase zinc-blende form with lattice parameter and optical energy gap values measured [12] and plotted in Figures 5 and 6.

The alloys of $z = 0.2$ and $z = 0.25$ appeared mainly two phase ($\alpha + \gamma$) but also showed the presence of small amounts of the single α or β phases respectively. For these non-equilibrium samples, a value of the lattice parameter a for the weak single phase conditions was still obtained even though there was considerable difficulty in distinguishing between zinc-blende and chalcopyrite phases with the same a value. However, another $z = 0.20$ sample similarly treated at 650°C but sealed in a thinner

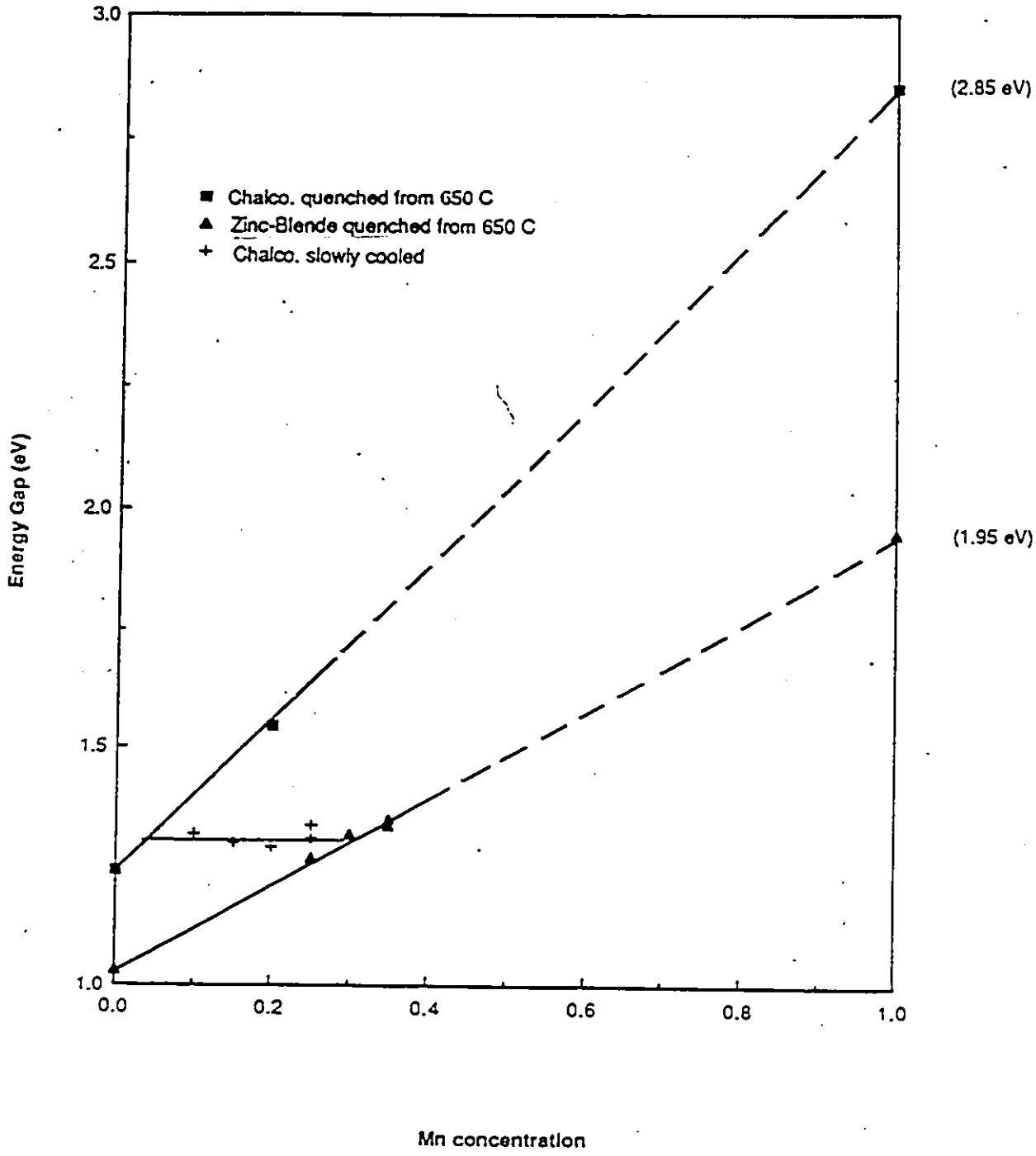

Figure 6: Variation of room temperature optical energy gap E_o with concentration z for $(CuGa)_{1-z}Mn_{2z}Te_2$ alloys.

tube was found to be, after quenching, of single phase chalcopyrite structure. For this reason, it is assumed that the α phase must extend beyond $z = 0.20$ in the neighborhood of 600°C. Thus, the boundary between the α and $(\alpha + \gamma)$ fields has been drawn as shown in Figure 3.

From Figure 5, we see that the values of a (whether for the zinc-blende or chalcopyrite phase) lie on a straight line within experimental error limits which extrapolates to a value of $a = 6.335\mathring{A}$ at $z = 1.0$. This is in good agreement with the corresponding values obtained previously [16] for the $(CuIn)_{1-z}Mn_{2z}Te_2$ and $(AgIn)_{1-z}Mn_{2z}Te_2$ alloys. The intersection of the a versus z curves of the single phase chalcopyrite α and two phase $(\alpha + \gamma)$ gives the limit of solid solubility in the α phase at 200°C. This limit seems to lie between $z = 0.03$ and $z = 0.04$. This value agrees with the solubility limit of $MnTe$ in $CuGaTe_2$ suggested by Aresti et al. [2].

For samples water quenched from 650°C, which appeared to be single phase cubic β in the x-ray photographs, major cusps occur in the susceptibility versus temperature curve. This showed that ordering of the Mn was occuring as will be discussed in detail in Chapter 4.

$(AgGa)_{1-z}Mn_{2z}Te_2$ Phase Diagram

The proposed phase diagram of the $(AgGa)_{1-z}Mn_{2z}Te_2$ alloy system is shown in Figure 4.

For samples cooled slowly to room temperature after annealing, their structures were determined from x-ray photographs taken during this work and previously by

Munkid Al Najjar [1] to be either single phase chalcopyrite or two phase (chalcopyrite and hexagonal $MnTe$) structures. Thus, no zinc-blende field exists at lower temperatures.

Lattice parameter values for the chalcopyrite phase of different compositions show that the variation of a with z was of the same magnitude as the experimental scatter in the data. In this case, the usual method of finding the limit of single phase field using the discontinuity of the a versus z curve cannot be used. Optical energy gap data [1] indicates that the $z = 0.5$ alloy is single phase while x-ray photographs of the $z = 0.6$ sample clearly show two phases. Thus, the phase boundary at lower temperatures in Figure 4 has been taken at $z = 0.55$.

2.4 Conclusion

The results obtained for the $(AgGa)_{1-z}Mn_{2z}Te_2$ alloys show that solid solutions of zinc-blende and chalcopyrite have a wide range ($0 \leq z \leq 0.55$) and that Mn-ordering in both structures occur in the 300°C–400°C temperature range.

The $(CuGa)_{1-z}Mn_{2z}Te_2$ alloys show a very narrow solid solubility range of about $0 \leq z \leq 0.04$ at $\sim$ 200°C with no Mn-ordered zinc-blende or Mn-ordered chalcopyrite phase in the equilibrium diagram. The DTA data also indicated that a 600°C annealing temperature for this system was probably not a good choice but samples annealed at different temperatures were found to give the same DTA data. It appears through magnetic susceptibility measurements that, for rapidly quenched samples of this alloy, metastable phases do occur in different proportions according to quenching conditions.

Depending on the amount of phases present, an extrapolation of the energy gap value E_o and of the magnetic transition temperature T_m versus z curve for both systems would give the position of the phase boundaries and the phase state of the sample respectively. All extrapolated values agree with previous measurements made on other alloy systems [1,12,16].

The positions of phase boundaries, especially those between two phase and single phase fields, were found through discontinuity in the lattice parameter a versus composition z curve where possible.

The results indicate that ordering of the manganese ions on the cation sublattice occurs in these alloys. Aresti et al. [2] have determined a phase diagram of the $(CuIn)_{1-z}Mn_{2z}Te_2$ system but did not obtain any indication of ordering temperatures, etc. They suggest that in the range of chalcopyrite behavior, the Mn tends to order on a stannite type of arrangement. Earlier work performed at Merida [17] support this suggestion. The proposed ordered structures of the $(AgGa)_{1-z}Mn_{2z}Te_2$ and $(CuGa)_{1-z}Mn_{2z}Te_2$ systems will be dealt with in more detail in later chapters.

Chapter 3

Magnetic Behavior

3.1 Theory of Magnetic Susceptibility

When an electron is bound to a nucleus, it possesses a magnetic moment due to its spin and orbital angular momenta. For atoms with more than one electron, it is necessary to consider the combination of all the spin and orbital momenta.

When the vector addition of the quantum numbers is complete, there exists only partially filled electronic levels possessing a non-zero resultant momentum. As an example, the five unpaired 3d electrons of Mn results in a value of spin momentum, S, equal to $\frac{5}{2}$. Because of this, only atoms such as Mn can have a net magnetic moment.

According to their magnetic properties, materials may be classed into three general categories;

1. Diamagnetic
2. Paramagnetic

One method to distinguish between them is to observe their response in an applied magnetic field. This is known as magnetic susceptibility measurements.

3.1.1 Susceptibility of Diamagnetics and Paramagnetics

For diamagnetic materials, this magnetic susceptibility, which is defined as

$$\chi = \frac{M}{H} \tag{5}$$

where M is the magnetization

and H is the applied magnetic field,

is negative and independent of temperature.

Paramagnetic systems have a positive susceptibility. At high temperatures and in small magnetic fields, they follow the Curie law:

$$\chi = \frac{Ng^2\mu_B^2 J(J+1)}{3k_B T} = \frac{C}{T} \tag{6}$$

where C is the Curie constant,

N is the number of magnetic ions,

k_B is the Boltzman constant,

T is the temperature in Kelvin,

g is the spectroscopic splitting factor

and J is the total angular momentum quantum number.

Paramagnetism arises from the random orientation of permanent magnetic dipoles.

When a magnetic field is applied there is a net dipole moment in the direction of the field giving rise to a weak magnetization or paramagnetism. When dipole-dipole interaction is negligible, experiment shows that paramagnetic materials obey Curie's law defined by Equation 6.

However, when dipole-dipole interaction is not negligible, the material's susceptibility can be fitted to the equation:

$$\chi = \frac{C}{T - \theta} \tag{7}$$

where θ is the Curie-Weiss temperature and is a constant which depends on the interaction between atomic magnetic moments. At low temperatures, this interaction may result in some kind of correlation amongst the various moments in the lattice.

3.1.2 Magnetic Susceptibility of Exchange Coupled Systems

Exchange coupled systems possess the common feature of having interaction between the atomic magnetic moments that result in some kind of alignment or correlation among the spins of the lattice. The coupling occurs through an exchange interaction which is a purely quantum mechanical phenomenon. It arises from the Pauli Exclusion Principle and from the indistinguishability of the electrons and depends on the overlap of the electronic wave functions.

The category of exchange coupled systems can be split into three important classifications:

1. Ferromagnetic Materials
2. Antiferromagnetic Materials
3. Ferrimagnetic Materials

Ferromagnetic and Antiferromagnetic Materials

When the atomic moments are aligned parallel, then the material is said to be ferromagnetic. As a result, at low temperatures a spontaneous magnetization exists in the material. Above a certain critical temperature T_c, the ferromagnetic Curie temperature, the thermal agitation overcomes the exchange forces and the alignment is lost. In this state, the material behaves like a paramagnet. At high temperatures and in small magnetic fields, the susceptibility may be described by Equation 7 where θ is the ferromagnetic ordering temperature and is positive.

When an antiparallel arrangement of the strongly coupled magnetic dipoles producing no net spontaneous magnetization is favoured, the material is said to be antiferromagnetic. In this case, the sublattices have antiparallel magnetizations that are equal and thus results in no net magnetic moment. Above a certain critical temperature T_N, the Néel temperature, the antiparallel alignment is lost and the material assumes a paramagnetic like state. At high temperatures and in a small magnetic field, the susceptibility is also described by Equation 7 but with the Curie-Weiss temperature θ being negative.

Ferrimagnetic Materials

When an antiparallel arrangement of the strongly coupled atomic dipoles give a spontaneous magnetization below a certain temperature, the material is said to be ferrimagnetic. In this case, the sublattices have antiparallel magnetizations that are

not equal resulting in a net magnetic moment. It should be noted that the susceptibility can resemble those of the ferromagnetic and antiferromagnetic materials at different temperatures.

We see that in all three of the cases discussed, the susceptibility at a high temperature above any ordering point and in a small magnetic field is described by Equation 7 with θ indicating the type and strength of the exchange interaction. A positive value means that the exchange is positive and the interaction is ferromagnetic while a negative value denotes a negative exchange and antiferromagnetic behavior.

Over the last two decades another distinct magnetic state known as spin glass has been recognized. The name "spin glass" was first introduced by B. Coles [6] to denote "the entire class of random magnetic alloys of moderate dilution in which the magnetic structure no longer resembles that of pure metals". In these materials, the spins interact with each other in such a way that when the temperature is low enough for this interaction to overcome the thermal agitation, the spins freeze into a completely random configuration. The absence of long range order from the coupling is what makes this spin glass very different from the above mentioned systems. A new concept, "frustration", was suggested by Toulouse [19] to explain the behavior in spin glass materials.

Where there is a conflict in the interaction between spins, frustration occurs. In a typical SMSC, magnetic ions distributed at random over the fcc sublattice interact antiferromagnetically with each other. For each magnetic ion, these interactions result in contradicting demands concerning their spin directions. A spin that tends to be aligned in a certain direction due to the influence of the nearest neighbor

could be acted upon by another nearest neighbor in an opposite direction. This is the result of the random distribution of the Mn within the sublattice. Therefore, when the temperature is smaller than T_g, the spin glass temperature, an equilibrium position of the spins is reached where all the magnetic ions are frozen in random orientations. The random freezing of spins at T_g was confirmed by Mössbauer effect [13] and neutron diffraction experiments [14].

In spin glass materials, the magnetic susceptibility measurements show a cusp like peak at a well defined temperature T_g and the behavior is similar to an antiferromagnetic. Above T_g the thermal processes overcome the freezing and a paramagnetic behavior occurs. In order to understand this spin glass behavior, one has to know the nature of the interactions between the spins.

3.2 Theory of Electron Spin Resonance

A free ion with a permanent magnetic moment has a resultant angular momentum quantum number J with $2J+1$ different degenerate levels. The application of a static field will lift this degeneracy and give $2J+1$ different levels having an energy:

$$E = M_J g \mu_B H \tag{8}$$

where M_J is the magnetic quantum number,

μ_B is the Bohr magneton,

H is the applied magnetic field

and g is the spectroscopic splitting factor.

This effect is known as Zeeman splitting.

When this ion is not free and forms part of a crystalline solid, its angular momentum is described only by the spin quantum number S because the total orbital momentum quantum number L is quenched, i. e. L=0. The application of a field H will produce a splitting of the $2S+1$ levels each with an energy $E = M_S g \mu_B H$. This g value is different from the Landé value because of the perturbing effect of the crystalline field on the orbital angular momentum of the ion.

As mentioned above, the crystalline field shifts some of the degenerate levels. This can be explained by the fine splitting. If we take the Mn^{2+} ion for example, it has a ground state which is sixfold degenerate classified as ${}^6S_{5/2}$. When such an ion is placed in a crystalline environment, where the concentration of Mn^{2+} is very small so that interaction between these ions is negligible, the free ion ground state sixfold splits into two levels. The upper level is fourfold degenerate and the lower is twofold degenerate. A magnetic field will lift the degeneracy of the doublet and quartet.

There are additional interactions to be considered. Since the nucleii possess an intrinsic spin angular momentum, the electron spin magnetic dipole will interact with it. Magnetic nucleii have corresponding multiplicity of nuclear spin states of $2I+1$ where I is the spin quantum number. This coupling of the nuclear magnetic and electron moments produce extra splitting at each level. This is known as the nuclear hyperfine interaction.

3.2.1 Effects of Applied Magnetic Field

In Electron Spin Resonance, (ESR), transitions between these energy levels can be induced by the application of an electromagnetic oscillating field whose energy $\hbar\omega$

is :

$$\hbar\omega = -g\mu_B H \tag{9}$$

where all the terms have the same meaning as previously stated. Resonance may be observed by fixing the frequency ω and varying H or vice versa. In normal ESR, the former is used with the frequency fixed at some point in the microwave range.

A selection rule from quantum mechanics operates so that only the transition between adjacent levels for which $\Delta M_S = \pm 1$ are possible. If the photon energy $h\nu$ matches the energy level separation, then Equation 9 meets the resonance condition.

However, in the materials being studied, there is the additional effect of the fine and hyperfine structure to be considered. Transitions between the degenerate levels of the fine structure in an applied magnetic field will produce five resonant lines in the ESR spectra. Because of the additional hyperfine coupling in the magnetic ion, the resonance spectrum is again split into six sets of the quintet mentioned above.

In general, the absorption does not occur at a sharply defined magnetic field. Instead it is spread out over a range of H. The size of the spread may be related to several different effects including various relaxation phenomena such as spin-spin and exchange interaction [20,21]. Also, a factor which may affect this linewidth, ΔH, is inhomogeneous broadening. This broadening is a result of the overlapping of any fine or hyperfine structure due to the presence of inhomogeneous fields in the crystal.

ESR has also been found to be a very useful technique to study the different relaxation processes and the spin-spin interaction. These properties can be revealed further by studying the positions and widths of the resonance lines as the temperature is varied.

3.3 Experimental Measurements and Results

3.3.1 Experimental Set-up

The magnetic susceptibility measurements were made using a SQUID magnetometer with magnetic fields in the range of 10 to 25 G, and over a temperature range of 4.2 to 250 K. The results allowed values of transition temperature T_c and the Curie-Weiss 'paramagnetic' temperature θ to be determined. ESR measurements were also made, a symmetric Mn^{2+} resonance line with 'g' value of 2.0 being observed at room temperature for each sample and the linewidth ΔH was measured as a function of temperature in the range 10 to 500 K, at X band microwave frequency ($\approx$9.4 GHz). The first derivative pattern of the resonance line was recorded and the peak to peak linewidth ΔH measured with a gaussmeter. Both experimental set-ups are described in more detail in the thesis of other members of the group at the University of Ottawa [5,8].

3.3.2 Results

The results from work done by Woolley et al. [24] indicate that the manganese atoms are distributed at random on the cation sites for chalcopyrite materials but that at room temperature the manganese can show crystallographic ordering. A good investigation of the behavior and arrangement of the ordered structure in the chalcopyrite range would require an almost completely ordered sample.

In the present work, magnetic susceptibility and ESR measurements were made on the $(AgGa)_{1-z}Mn_{2z}Te_2$ and $(CuGa)_{1-z}Mn_{2z}Te_2$ systems with compositions within the zinc-blende and chalcopyrite ranges. Some measurements showed that

the samples exhibited only a certain degree of crystallographic order of the Mn atoms on the appropriate lattice with other phases also present. It was found that the ESR curve was more sensitive to the presence of two phases and so room temperature ESR measurements were mostly used to check the condition of each sample.

To begin with, two samples of $(AgGa)_{1-z}Mn_{2z}Te_2$ of composition $z = 0.4$, which had been prepared as described in Chapter 2, were annealed at 600° C. One sample was quenched rapidly in water and the other left to cool slowly in air down to room temperature. When the curves of magnetic susceptibility χ versus temperature for both samples were studied, it was found that one fairly strong peak was observed corresponding to some transition temperature, but that secondary smaller peaks were also found. Also, from the ESR spectra for each sample, it was found that a combination of two lines, one broad and one narrow, was observed rather than the single line expected. The relative amplitude of the peaks in the susceptibility measurement and the lines in the ESR spectra depended on the rate of cooling from the annealing temperature.

The dependence of the amplitude of the peaks is illustrated by the curve of χ versus T shown in Figure 7 for the samples of $(AgGa)_{1-z}Mn_{2z}Te_2$ where $z = 0.4$ and annealed at 600° C and (a) quickly quenched in water and (b) left to cool slowly in air. Curve (a) shows a major cusp at 35 K with small subsidiary peaks at 6 K and 63 K. Curve (b) shows the major cusp at about 38 K with a subsidiary peak at 65 K and the appearance of another peak at 12 K.

These peak temperatures, T_m, are shown in Figure 8 together with the corresponding values from other quenched samples obtained by other members of the

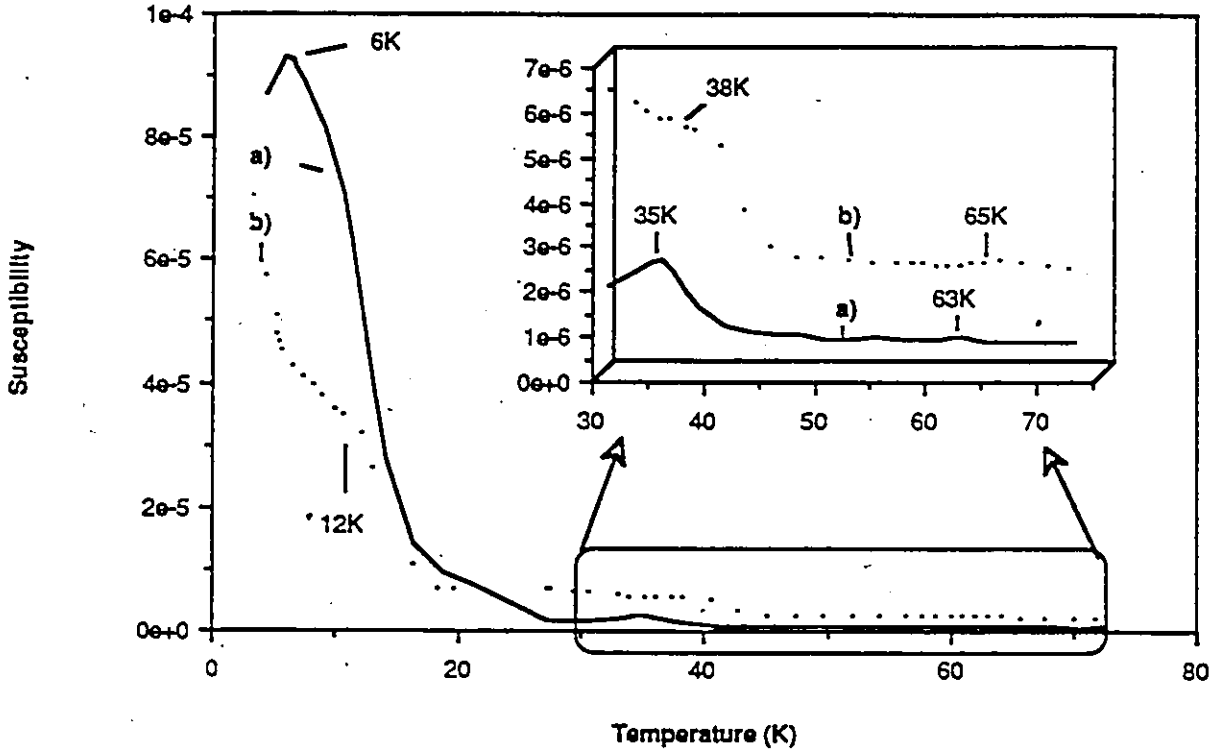

Figure 7: Temperature dependence of the magnetic susceptibility for samples of $(AgGa)_{1-z}Mn_{2z}Te_2$ with $z = 0.4$ and (a) quickly quenched in water and (b) cooled slowly in air.

group [24]. It is seen that the points fall on four separate lines, which, as shown previously [24], can be attributed, in descending order of T_m, to Mn-ordered chalcopyrite, Mn-ordered zinc-blende, Mn-disordered zinc-blende and Mn-disordered chalcopyrite. The scatter in points for the samples of any composition is probably due to variations in the degree of order in the samples rather than to different chemical composition.

The results together with those from ESR measurements indicate that the sample water quenched from single phase β field at 600° C contains some amounts of three possible single phase structures at $z = 0.4$. The size of the peak in the χ

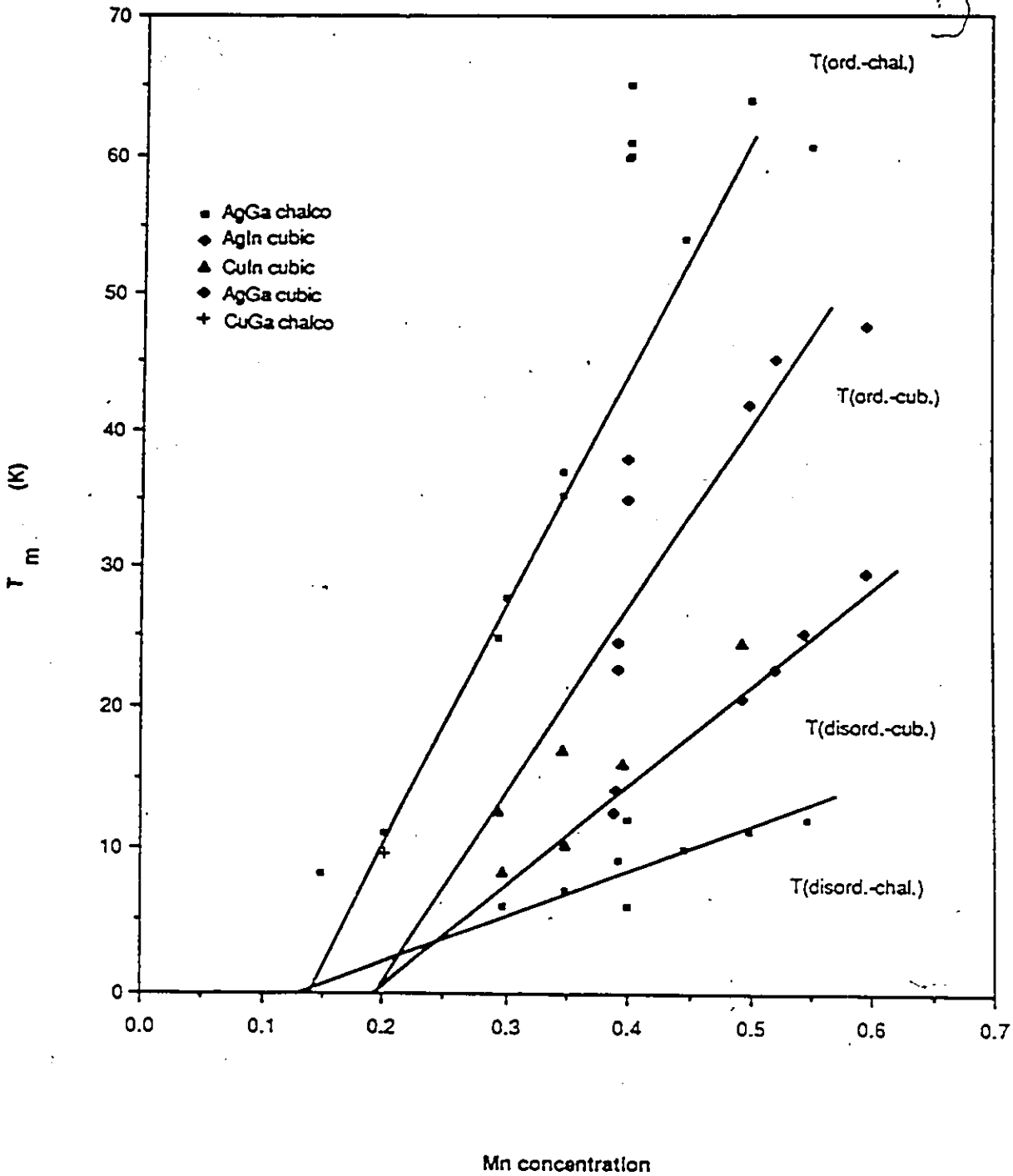

Figure 8: Values of T_d and T_o versus Mn concentration z from magnetic susceptibility results of the samples indicated.

vs T curve indicates that the cubic material in the sample is mainly Mn-ordered. However, the susceptibility data also indicate the presence of a small amount of the Mn-ordered chalcopyrite phase and probably a still smaller amount of the Mn-disordered chalcopyrite phase. Although the phase diagram of $(AgGa)_{1-z}Mn_{2z}Te_2$ does not contain any Mn-disordered chalcopyrite phase at $z = 0.4$, it is possible that any Mn-disordered zinc-blende material quenched into a Mn-ordered chalcopyrite field (thus not being in equilibrium) will tend to rearrange itself into Mn-disordered chalcopyrite.

For the sample that had been left to cool slowly in air, having initially undergone annealing at 600° C, a major peak at 38 K (Figure 7) indicates a large amount of Mn-ordered zinc-blende and the little-peaks at 65 and 12 K show the presence of smaller amounts of Mn-disordered zinc-blende and Mn-ordered chalcopyrite. The presence of these phases is consistent with the equilibrium diagram of Figure 4 in Chapter 2 at $z = 0.4$.

Thus, it was concluded that by quenching at a proper cooling rate, the sample was able to keep a good equilibrium condition right down to room temperature and retain some of the phases it passed thru. A "completely" Mn-ordered $(AgGa)_{1-z}Mn_{2z}Te_2$ sample of $z = 0.4$ could conceivably be obtained by annealing the sample at 200° C within the α' region of the T(z) diagram (Figure 4 in Chapter 2).

A $z = 0.4$ sample of the above mentioned system was annealed within the temperature range (200° C) expected to induce the Mn-ordered chalcopyrite phase. Magnetic susceptibility measurements on this sample showed the presence of only one discernable peak at $T_m = 61$ K as shown in Figure 9. Using the results shown

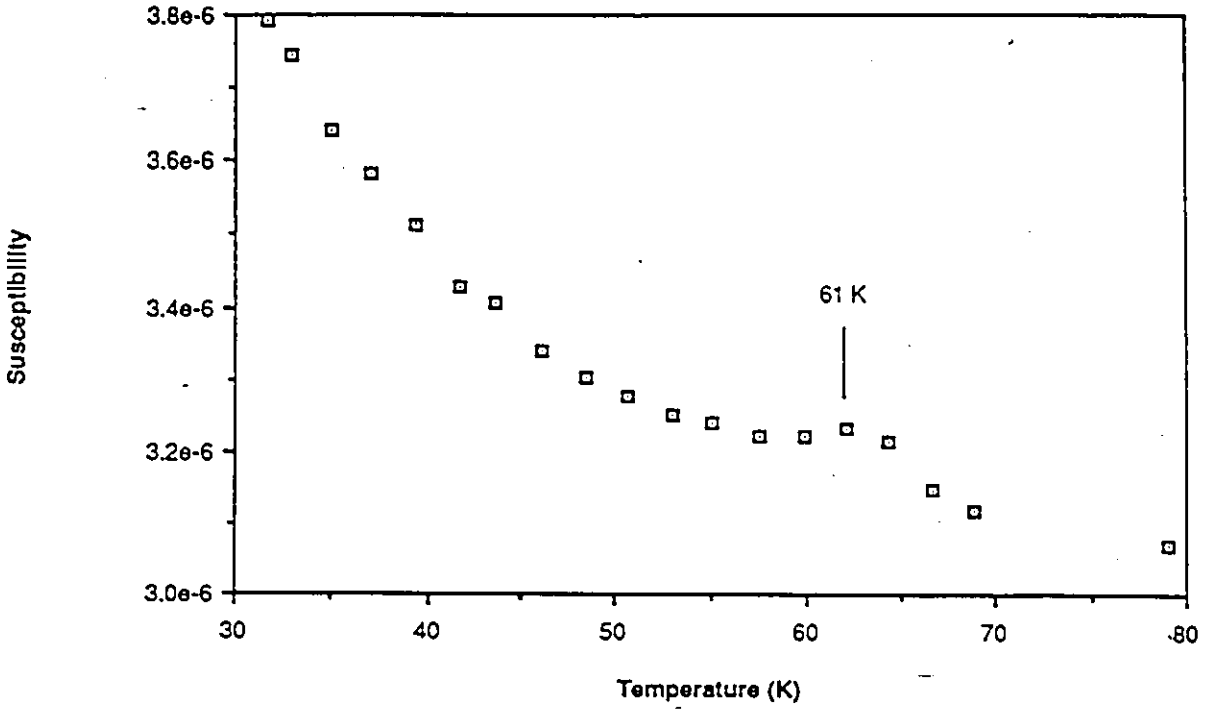

Figure 9: Magnetic susceptibility of $(AgGa)_{1-z}Mn_{2z}Te_2$ sample with $z = 0.4$ annealed at 200° C.

previously [24], it seems that only the Mn-ordered chalcopyrite phase is present. This was corroborated by the fact that an ESR spectra of this sample indicated only one narrow line, which has been previously associated with ordered structures.

Various ESR measurements were made during the present work with energy gap measurements made by Roger Goudreault [12] on various compositions of the $(CuGa)_{1-z}Mn_{2z}Te_2$ system. All measurements were performed before the T(z) phase diagram (Figure 3 in Chapter 2) was available. Preliminary energy gap and magnetic susceptibility measurements made by R. Goudreault while working on his Master's thesis at the University of Ottawa had indicated that samples of $z = 0.2$ composition of this system which had been rapidly quenched from 650° C down to room temperature could be of the Mn-ordered chalcopyrite structure.

The χ versus T diagram of this sample showed only one peak of medium intensity at $T = 10$ K. When plotted on the T_m versus z diagram (Figure 8) as done previously [24], the samples' structure was determined to be Mn-ordered chalcopyrite. ESR spectra taken during the present work on the above mentioned sample gave only one narrow line, again indicating an ordered structure. However, as seen from the T(z) diagram (Figure 3 in Chapter 2) and as will be shown by neutron diffraction measurements, the equilibrium condition of this sample is two phase.

3.4 Discussion and Conclusion

The results stemming from the present work agrees with similar previous results [24] and indicates that the manganese atoms in the chalcopyrite and cubic structures are distributed at random on the cation sublattices at high temperatures. We also see that the manganese tends to order within the lattice at lower temperatures. This is again consistent with previous measurements performed on similar systems [17] that showed ordered fields at lower temperatures on their phase diagrams.

It is clear from the degree of ordering present in the $(AgGa)_{1-z}Mn_{2z}Te_2$ sample of composition $z = 0.4$ that was slowly cooled, that a longer annealing period within an ordered field would produce more ordered material within the sample. This is shown by the results from the sample that had been annealed at 200° C, which was found to be of single phase Mn-ordered chalcopyrite structure.

The initial measurements of magnetic susceptibility and ESR [12] on the $z = 0.2$ sample of $(CuGa)_{1-z}Mn_{2z}Te_2$ indicated that an ordered structure was present, in that from the susceptibility T_m values lying on the Mn-ordered line of Figure 8 were

observed and also in the narrow line for ESR. Hence samples were set to anneal at 300° C to enhance the ordered form with the aim that these would be used for neutron diffraction work. Only after the neutron diffraction measurements had been started did the T(z) data for this system become available and this combined with the results of the diffraction work clearly showed that the equilibrium condition at 300° C was two phase as indicated in Figure 3 in Chapter 2. It is clear that the ordered form initially observed represented high temperature phases which were still present after cooling from 600° C. These phases would be lost after the long anneal at lower temperatures.

In view of the initial results given above, nine gram samples of $z = 0.2$ of the $(CuGa)_{1-z}Mn_{2z}Te_2$ system and $z = 0.4$ of the $(AgGa)_{1-z}Mn_{2z}Te_2$ systems were annealed for a long period at 300° C and 200° C, respectively, and were used later for neutron diffraction measurements. The choice of these two particular systems for neutron work will be made clear in the next chapter.

3.4.1 Possible Ordered Structures

Since no extra ordering lines have been observed on the x-ray results for both systems, a possible ordering scheme is that the manganese atoms enter only the I or III sublattices, allowing the other sublattice to accept the displaced atoms, as suggested by Woolley et al. [24]. In the case where very faint ordering lines have been observed in a similar system [16], it has been suggested [2] that Mn-ordered chalcopyrite field have a "stannite" type structure. If you characterize the α field by two extremal structures, chalcopyrite at $z = 0$ and stannite at $z = 0.5$, the differing degrees of order can be attributed to periodic structures realized by

entirely replacing the planes of the chalcopyrite structure by Mn atoms. The many compositions (z) would consists of suitably alternated (I, III) and Mn planes.

To investigate this ordering more closely, neutron diffraction measurements would be taken during this work to locate the positions of the Mn within the ordered chalcopyrite lattice. Other samples of varying compositions were also made during this work in view of future neutron work to be performed by Riccardo Brun del Re [4].

Chapter 4

Neutron Diffraction

4.1 Introduction

The small velocities of thermal neutrons makes possible the investigation of atomic motion in crystals. The specific applications of neutron diffraction can be reasoned from the general types of interaction of x-rays and neutrons with physical matter. Because of the neutron's magnetic moment, the determination of the arrangement of the magnetic moments in magnetically ordered materials is possible. The determinations of magnetic structure are largely based on symmetry considerations which are an exciting development of the classical methods in crystallography.

4.2 Theory

4.2.1 The Neutron Advantage

The neutron has been used in scattering experiments on crystalline solids since 1946. Neutrons have no electrical charge, a mass almost equal to that of the proton, a nuclear spin of 1/2 and a magnetic moment. Since the thermal neutron has a wavelength of the same order as the lattice spacing, the technique of Bragg reflection can be used to obtain beams having a sharp energy.

The preferential Bragg reflection condition is;

$$m\lambda = 2d\sin\phi \tag{10}$$

where λ is the wavelength corresponding
to the sharp energy E_n,
m is the order of the reflection
and d is the lattice spacing.

The neutron energy for a first-order Bragg reflection is essentially determined by the angle of incidence ϕ and is given by;

$$E_n = \frac{h^2}{8m_n d^2 \sin^2\phi} \tag{11}$$

where m_n represents the neutron's mass. Since the de Broglie wavelength of neutrons ranges from about $\lambda = 0.1$ to 10Å, over the energy interval $E_n = .001$ to 10 eV, they lend themselves to diffraction studies of the structure of materials with

techniques akin to those developed for x-ray work.

However, there is one fundamental distinction between the two methods. Whereas x-ray scattering takes place on the electrons of the atoms in the crystals, the coherent scattering of thermal neutrons takes place on the nuclei. Important consequences arising from this distinction are;

- Because slow-neutron scattering cross-sections have roughly the same magnitude for all elements, there is no differentiation between light and heavy element scattering as one finds with x-rays.

- Since the neutrons possess a spin and some target atoms possess a magnetic moment, the scattering intensity will depend on a) the orientation of the nuclear spins and b) the relative orientations of the neutron spin and magnetic moment, if the scattering interaction is spin dependent. X-ray scattering is altogether independent of atomic orientation.

- Neutron diffraction effects are much more sensitive to surface characteristics. This is due to much higher absorption cross-sections than that of x-rays.

Neutron diffraction therefore makes it possible to find the positions of the atomic nuclei and is an important complement to x-ray diffraction methods.

4.2.2 Neutron Diffraction Technique

The Debye-Scherrer x-ray powder diffraction technique is also applicable to neutron diffraction. It consists of producing and analyzing the diffraction pattern of a monoenergetic thermal neutron beam. One determines the structure of the pattern

with a neutron detector mounted facing the target and free to swivel about it. The position of the intensity maxima that correspond to different orders of Bragg reflection from various lattice planes can be established. The peaks are then labelled according to the respective Miller indices of the crystal planes from which reflection occured.

A crystal lattice is characterized by a set of interplanar distances d_{hkl} given by the quadratic form;

$$\frac{1}{d_{hkl}} = f(\underbrace{a,\ b,\ c}_{\substack{unit\ cell \\ periods}},\ \overbrace{\alpha,\ \beta,\ \gamma}^{\substack{angle\ bet. \\ coord.\ axes}}) \tag{12}$$

The angular position of a particular maximum in the pattern is given by the Wulff-Bragg equation;

$$\lambda = \frac{2d_{hkl}}{m} \sin\theta_{hkl} \tag{13}$$

Because a number of different planes all contribute to a single maximum due to equivalent interplanar distances, it is sufficient to determine the contribution of any one of the equivalent planes to the intensity of a particular maximum and then multiply by the recurrence factor j_{hkl}. We must also consider the scattering power of the unit scattering entity and interference effects in the atom when estimating a reflected beam's intensity.

The scattering power of each center is characterized by an atomic scattering amplitude f; f^n for nuclear neutron scattering and f^m for magnetic neutron scattering. This important parameter is dependent on the magnitude of the permissible values

for the energy of the nucleus or, more precisely, of the compound nucleus formed from the incident neutron and the target nucleus. The contribution to the scattering from this resonance effect varies haphazardly from atom to atom in the Periodic Table. In the case of a few elements, such as hydrogen, titanium and manganese, the scattering amplitude is negative. This means that, in addition to neutrons being scattered as with most nuclei, there is an additional phase change of π. Since with x-rays it is difficult to distinguish Mn from other neighboring elements in the Periodic Table, this resonance-like effect in manganese is the main reason that neutron diffraction measurements are being used to investigate crystallographic ordering in our systems.

4.2.3 The Structure Factor

The intensity of each reflection for all forms of scattering is related to the structure of the atoms in the unit cells of the target by way of the structure factor, $\mathcal{F}_{hkl}$. The structure factor can be expressed as;

$$\mathcal{F}_{hkl}^2 = \left(\sum_{\nu}^{unitcell} f_\nu \cos 2\pi(hx_\nu + ky_\nu + lz_\nu) \right)^2 + \left(\sum_{\nu}^{unitcell} f_\nu \sin 2\pi(hx_\nu + ky_\nu + lz_\nu) \right)^2 \tag{14}$$

where x_ν, y_ν and z_ν are parameters determined by the position of the scattering center ν and f_ν is the corresponding atomic scattering amplitude.

The case of magnetic scattering is much more complicated and involves many vector relationships. The magnetic scattering structure amplitude also differs from

its analog in nuclear scattering in that the summation extends only over the magnetic atoms and not all the atoms in the unit cell. The relative orientation of the magnetic moments must also be taken into account by the sign of f_ν. Its structure factor is thus expressed by;

$$\mathcal{F}^2_{hkl} = \left(\sum_{\nu}^{unitcell} \pm f_\nu \cos 2\pi(hx_\nu + ky_\nu + lz_\nu) \right)^2 + \left(\sum_{\nu}^{unitcell} \pm f_\nu \sin 2\pi(hx_\nu + ky_\nu + lz_\nu) \right)^2 \tag{15}$$

The structure factor of any reflection for nonpolarized neutrons constitutes the sum of the nuclear and magnetic structure factors.

$$\mathcal{F}^2_{hkl} = \mathcal{F}^{2(nucl)}_{hkl} + \mathcal{F}^{2(magn)}_{hkl} \tag{16}$$

The present investigation of the crystallographic ordering did not include magnetic scattering considerations because neutron diffraction measurements were done at room temperature, well above the magnetic ordering temperatures of any of these materials. This work is not directed toward the observation of magnetic ordering but of crystallographic ordering in certain compounds. In our systems, the magnetically ordered structure will be investigated by other members of the group [4] which will require low temperature neutron diffraction measurements.

4.3 Experimental Set-up

In comparison with x-ray tubes, a nuclear reactor's flux is very small and for this reason neutron experiments must be optimized in order to attain the necessary resolution with the available flux.

The first possibility of optimization is fitting the spectral distribution of the neutrons to the experiment in question. One must limit the beam's angular divergence by means of a collimator and select a wavelength band by means of a monochromator. The necessary resolution is obtained with the help of collimators in the primary beam before the monochromator, between the monochromator and the sample and between the sample and the counter. For measurements on crystalline powders, one has to consider how the measurements should be carried out to obtain the best compromise between resolution and well-defined integrated intensities. The necessary incident neutron wavelength selection and appropriate beam collimation procedures were done by Dr. Tom Holden and Dr. David Noakes.

The experimental arrangement must be able to resolve some chalcopyrite Bragg peaks that have very close Bragg angles and also minimize the background at higher Bragg angles where the superlattice reflections tend to have weaker intensities.

Since the spectrometer used in the present investigation has a scanning capability of only $2\theta \simeq 110°$ scattering angle, a neutron beam monochromated by reflection on the (331) plane of a Si prism with a wavalength of $\lambda = 1.8787\mathring{A}$ was found to make the chalcopyrite reflections of Table 2 observable under a 110° scan. The search for the Si (331) plane reflecting the highest neutron flux for better diffraction intensity was undertaken. The Si $(33\bar{1})$ plane was found to reflect the highest neutron flux at the chosen wavelength.

Afterwards, the geometry of the set-up, e. g. collimation ratios of the neutron beam before and after the reflection from the sample, was organized. In this case, the resolution or FWHM (full width at half maximum), $A_{1/2}$, at different Bragg

angles is [10,7,22]

$$A_{1/2}^2 = U\tan^2\theta + V\tan\theta + W \tag{17}$$

where

$$U = \frac{4}{\tan^2\theta_{mono}}\left[\frac{(\alpha_1^2\alpha_2^2 + \alpha_1^2\beta^2 + \alpha_2^2\beta^2)}{(\alpha_1^2 + \alpha_2^2 + 4\beta^2)}\right]$$

$$V = \frac{4}{\tan^2\theta_{mono}}\left[\frac{(\alpha_1^2\alpha_2^2 + 2\alpha_2^2\beta^2)}{(\alpha_1^2 + \alpha_2^2 + 4\beta^2)}\right]$$

$$W = \left[\alpha_1^2\alpha_2^2 + \alpha_1^2\alpha_3^2 + \alpha_2^2\alpha_3^2 + 4\beta^2(\alpha_2^2 + \alpha_3^2)\right]$$

As shown in Figure 10, the collimators are positioned so that;

α_1: is the angular divergence between the pile and monochromator,

α_2: is the angular divergence between the monochromator and sample,

α_3: is the angular divergence between the sample and detector

and β: is the mosaic spread of the monochromating crystal.

For the present work, both α_1 and β were constants at 0.85° and 0.20° respectively, and the α_2 and α_3 collimation factors were varied to obtain the best possible compromise between resolution and intensity. By setting $\alpha_2 = 0.31°$ and $\alpha_3 = 0.3675°$, the resulting diffraction pattern would have a minimum resolution of $A_{1/2min} = 0.41°$ with a minimum in background occuring near the middle of the scan at a scattering angle of $2\theta_{min} \simeq 58°$. This would assure us of a reduced background intensity at higher scattering angles thus providing a clearer image of high-angle low-intensity Bragg peaks.

One of the restrictions imposed by the nature of the experiment was on the material to be analysed. Indium and cadmium, because of their high neutron absorption cross-sections, were not included in any system to be investigated by neutron diffraction. The $(CuGa)_{1-z}Mn_{2z}Te_2$ and $(AgGa)_{1-z}Mn_{2z}Te_2$ systems would be the

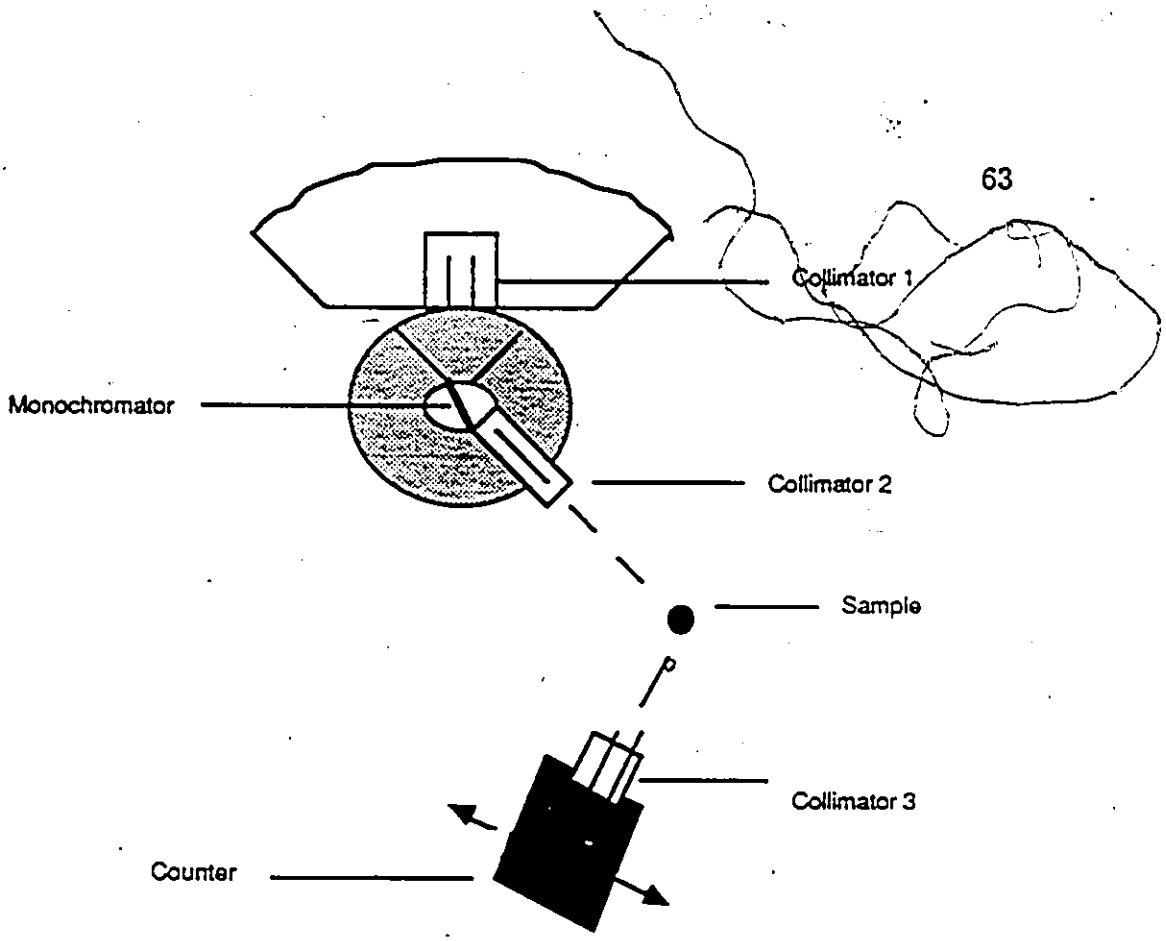

Figure 10: Schematic diagram of neutron beam collimation on diffractometer apparatus.

only alloys to be studied by this technique during this work.

The samples used were the $z = 0.2$ of the $(CuGa)_{1-z}Mn_{2z}Te_2$ system and the $z = 0.4$ of the $(AgGa)_{1-z}Mn_{2z}Te_2$ system that had been annealed, at 300° C and 200° C respectively. The powdered samples were put into aluminum cylindrical containers sufficiently small in diameter to be fully bathed in the neutron beam. Each sample was carefully positioned on the rotating table of the diffractometer at the start of each scan. The sample would rotate throughout the scan time so as to cover the whole range of plane orientations within the powdered sample in which there is any contribution to a particular reflection.

The counter was then programmed to scan a range of Bragg angles of $2\theta = 10°$ up to $2\theta = 110°$. The counting period used was approximately $2\frac{1}{2}$ minutes for

every $2\theta = 0.1°$. After approximately 44 hours, the data obtained was fed into a pen-recorder and a diffraction spectra was plotted and ready to be analysed.

4.4 Structure Amplitudes

As indicated in Chapter 2, the present work examines the chalcopyrite phases of both the $(AgGa)_{1-z}Mn_{2z}Te_2$ and $(CuGa)_{1-z}Mn_{2z}Te_2$ systems. In the chalcopyrite structure there are two cation sublattices each occupied by one type of cation and one anion sublattice. For the hypothetical system $(AB)C_2$ with an ideal chalcopyrite structure where A, B and C are the elements making up this structure, the atomic positions, (x_ν, y_ν, z_ν), of each atom within the lattice are given by;

$$\begin{aligned}
A \Rightarrow\ & (000)\ \ (\tfrac{1}{2}\tfrac{1}{2}\tfrac{1}{2})\ \ (\tfrac{1}{2}0\tfrac{1}{4})\ \ (0\tfrac{1}{2}\tfrac{3}{4}) \\
B \Rightarrow\ & (\tfrac{1}{2}\tfrac{1}{2}0)\ \ (00\tfrac{1}{2})\ \ (0\tfrac{1}{2}\tfrac{1}{4})\ \ (\tfrac{1}{2}0\tfrac{3}{4}) \\
C \Rightarrow\ & (\tfrac{1}{4}\tfrac{1}{4}\tfrac{1}{8})\ \ (\tfrac{3}{4}\tfrac{3}{4}\tfrac{1}{8})\ \ (\tfrac{3}{4}\tfrac{1}{4}\tfrac{3}{8})\ \ (\tfrac{1}{4}\tfrac{3}{4}\tfrac{3}{8}) \\
& (\tfrac{1}{4}\tfrac{1}{4}\tfrac{5}{8})\ \ (\tfrac{3}{4}\tfrac{3}{4}\tfrac{5}{8})\ \ (\tfrac{3}{4}\tfrac{1}{4}\tfrac{7}{8})\ \ (\tfrac{1}{4}\tfrac{3}{4}\tfrac{7}{8})
\end{aligned}$$

In the present systems, the anions are shifted by a small factor u from the ideal positions within the lattice. As discussed earlier in the chapter, each atomic site within the lattice has associated with it an atomic scattering amplitude f_A, f_B and f_C. By way of Equation 14 and by substitution of all the appropriate scattering amplitudes and lattice coordinates, we see that the structure factor, $\mathcal{F}_{hkl}$, which is related to the diffraction intensity, is non-zero only for reflections on types of planes having specific h, k and l combinations. Non-zero reflections occur at;

Type A $\Rightarrow$ h and k odd, l singly even

$$\text{where } \mathcal{F}^2_{(hkl)} = 16[(f_A + f_B)^2 + 4f_C^2]$$

Type B $\Rightarrow$ h and k even, l doubly even with $h+k+\frac{l}{2}$ singly even

$$\text{where } \mathcal{F}^2_{(hkl)} = 16[f_A + f_B - 2f_C]^2$$

Type C $\Rightarrow$ h and k even, l doubly even with $h+k+\frac{l}{2}$ doubly even

$$\text{where } \mathcal{F}^2_{(hkl)} = 16[f_A + f_B + 2f_C]^2$$

Type D $\Rightarrow$ h and k are one odd, one even, l is odd

$$\text{where } \mathcal{F}^2_{(hkl)} = 8(f_A - f_B)^2$$

All other conditions give $\mathcal{F}^2_{(hkl)} = 0$.

Type A, B and C reflections are known as the structure reflections from comparison to the cubic case and Type D as the chalcopyrite ordering reflections because of the ordering of the cations on the appropriate sublattices.

If we apply these structure factor equations to the alloy systems to be investigated ($(AgGa)_{1-z}Mn_{2z}Te_2$ and $(CuGa)_{1-z}Mn_{2z}Te_2$) in the case where the manganese is disordered (i. e. Mn enters the cation sites at random) in the chalcopyrite lattice, we obtain the four types of reflections described above but which now have a structure factor that depends on the manganese concentration z.

Type A $\Rightarrow$ $\mathcal{F}^2 = 16[(1-z)(f_{Ag/Cu} + f_{Ga}) + 2z{f_{Mn}}^2 + 4f^2_{Te}]$

Type B $\Rightarrow$ $\mathcal{F}^2 = 16[(1-z)(f_{Ag/Cu} + f_{Ga}) + 2zf_{Mn} - 2f_{Te}]^2$

Type C $\Rightarrow$ $\mathcal{F}^2 = 16[(1-z)(f_{Ag/Cu} + f_{Ga}) + 2zf_{Mn} + 2f_{Te}]^2$

Type D $\Rightarrow$ $\mathcal{F}^2 = 8[(1-z)(f_{Ag/Cu} - f_{Ga})]^2$

The $f_{Ag/Cu}$ factor indicates the appropriate scattering amplitude depending on which of the two systems we are dealing with. The structure factor values for

chalcopyrite of differing compositions for both systems are shown in Figure 11.

From the Mn-disordered structure of both systems, one must proceed to postulate the many possible ordering arrangements that the manganese can take within the lattice.

4.4.1 Proposed Mn-ordered Structures

One proposed Mn-ordering arrangement [24] within the chalcopyrite structure is where the manganese enters only one of the cation sublattices at random. In a neutron diffraction study, this arrangement leads to the observance of the structure reflections (Types A, B and C) with chalcopyrite ordering reflections (Type D) that now have a much greater intensity than in the Mn-disordered chalcopyrite case. This intensity change of the Type D reflection can be seen in its structure factor equation that now has a dependence , not only on the Mn concentration but also on the Mn scattering amplitude, f_{Mn}, as shown below for the case of Mn entering either the Cu/Ag or Ga sublattices at random. For the Type D chalcopyrite ordering reflections,

1) for the $(CuGa)_{1-z}Mn_{2z}Te_2$ system where Mn enters

a) Cu sublattice at random

$$\mathcal{F}^2 = 8[(1-3z)f_{Cu} - (1-z)f_{Ga} + 2zf_{Mn}]^2$$

b) Ga sublattice at random

$$\mathcal{F}^2 = 8[(1-3z)f_{Ga} - (1-z)f_{Cu} + 2zf_{Mn}]^2$$

2) for the $(AgGa)_{1-z}Mn_{2z}Te_2$ system where Mn enters

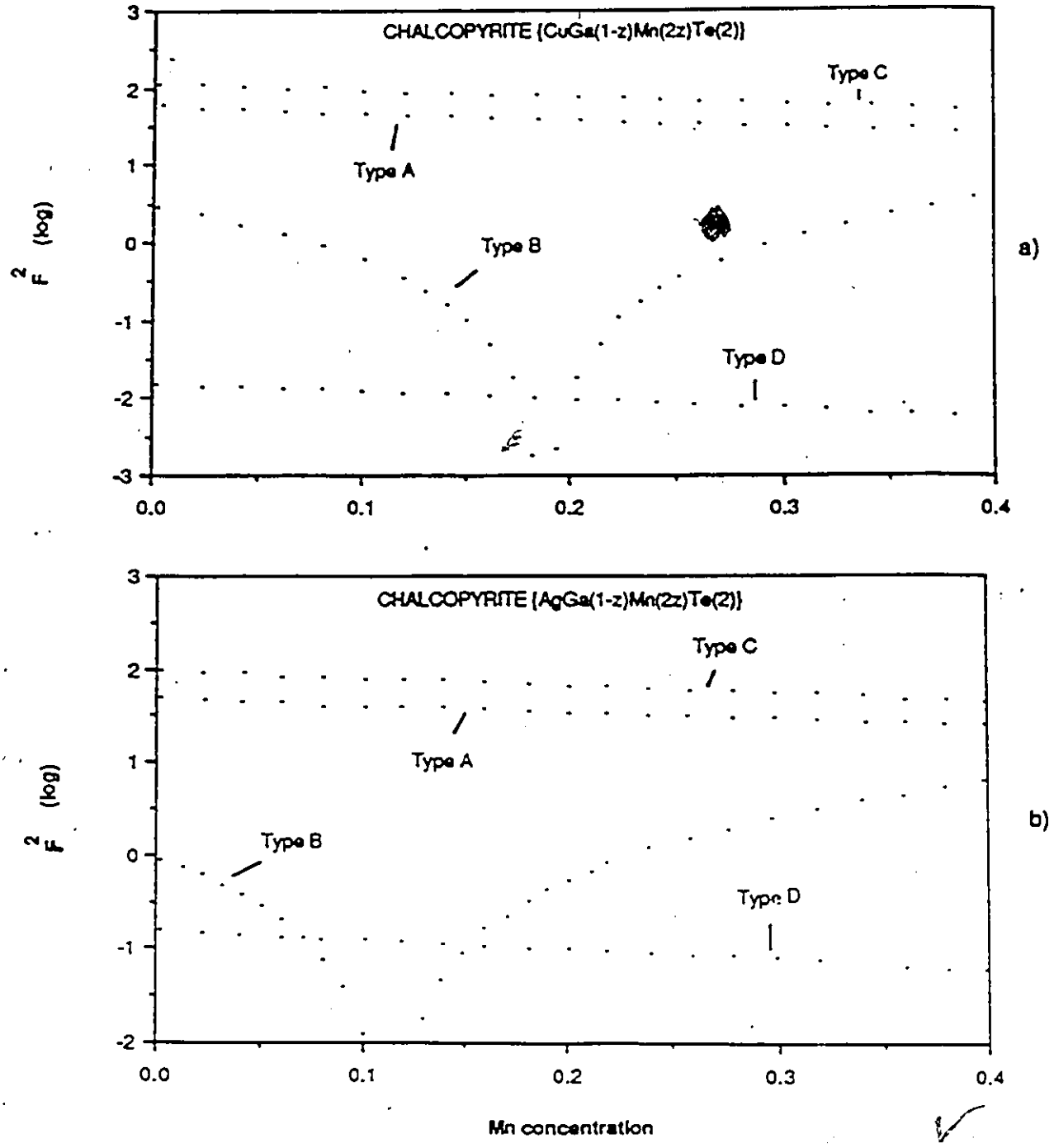

Figure 11: Structure factor values for the chalcopyrite structure where Mn is disordered on the cation sublattices for the a) $(CuGa)_{1-x}Mn_{2x}Te_2$ and b) $(AgGa)_{1-x}Mn_{2x}Te_2$ systems.

a) Ag sublattice at random

$$\mathcal{F}^2 = 8[(1-3z)f_{Ag} - (1-z)f_{Ga} + 2zf_{Mn}]^2$$

b) Ga sublattice at random

$$\mathcal{F}^2 = 8[(1-3z)f_{Ga} - (1-z)f_{Ag} + 2zf_{Mn}]^2$$

For the reflections of Type A, B and C, the structure factors remain equal to those of the Mn-disordered chalcopyrite case.

Thus, for manganese entering a chosen cation sublattice at random, the structure factors at different Mn concentrations for both systems behave as shown in Figure 12 for all structure reflections (Type A, B and C) and chalcopyrite ordering reflections (Type D).

Another possible ordering scheme for the manganese within the chalcopyrite lattice could result in the stannite-like structure as suggested by Aresti et al. [2]. Such crystal arrangement leads to the manganese entering, at random, both planes at height $\frac{1}{4}c$ and $\frac{3}{4}c$ which could be equally occupied by any one of the cations within the chalcopyrite lattice. In the present systems, the manganese would, at random, enter the Ag/Cu and Ga sites at planes of $\frac{1}{4}c$ and $\frac{3}{4}c$ height within the lattice. The atomic positions within the lattice for the ideal case of concentration $z = 0.5$ are;

$$\begin{array}{rllll}
Ag/Cu \Rightarrow & (000) & (\frac{1}{2}\frac{1}{2}\frac{1}{2}) & & \\
Ga \Rightarrow & (00\frac{1}{2}) & (\frac{1}{2}\frac{1}{2}0) & & \\
Mn \Rightarrow & (0\frac{1}{2}\frac{1}{4}) & (\frac{1}{2}0\frac{1}{4}) & (0\frac{1}{2}\frac{3}{4}) & (\frac{1}{2}0\frac{3}{4}) \\
Te \Rightarrow & (\frac{1}{4}\frac{1}{4}\frac{1}{8}) & (\frac{3}{4}\frac{3}{4}\frac{1}{8}) & (\frac{3}{4}\frac{1}{4}\frac{3}{8}) & (\frac{1}{4}\frac{3}{4}\frac{3}{8}) \\
 & (\frac{1}{4}\frac{1}{4}\frac{5}{8}) & (\frac{3}{4}\frac{3}{4}\frac{5}{8}) & (\frac{3}{4}\frac{1}{4}\frac{7}{8}) & (\frac{1}{4}\frac{3}{4}\frac{7}{8})
\end{array}$$

Using the structure factor equation, we find non-zero reflections occuring at six types of (hkl) combinations. We found that Type A, B and C reflections have the

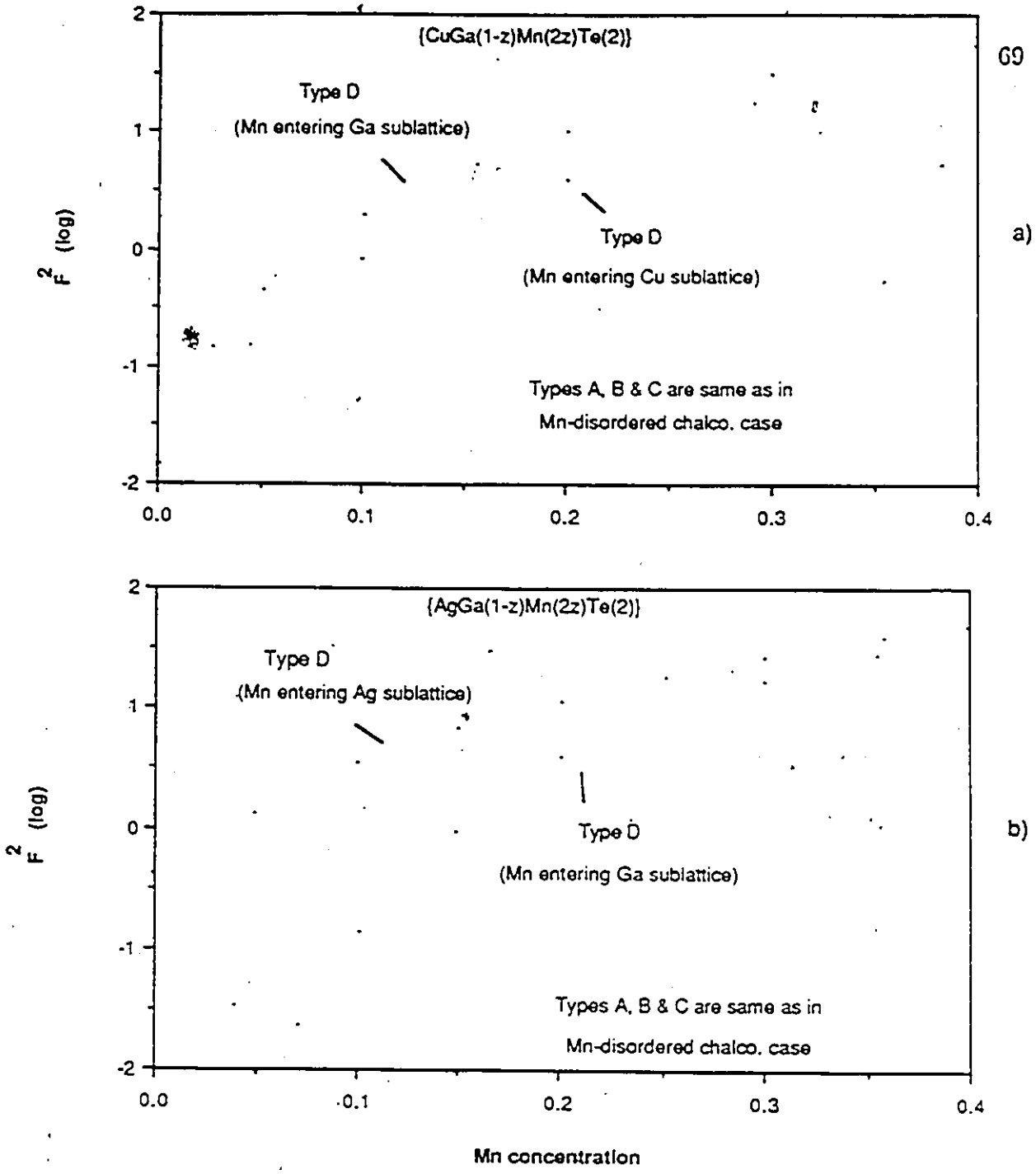

Figure 12: Variation of structure factors with concentration for the case where the Mn enters a preferred cation sublattice in the a) $(CuGa)_{1-z}Mn_{2z}Te_2$ and b) $(AgGa)_{1-z}Mn_{2z}Te_2$ systems.

same structure factors as that of the chalcopyrite structure. The Type D reflection has the same structure factor form as that of the chalcopyrite but is reduced in intensity. Two new reflections, Type E and Type F, occur in the stannite case due to the ordering of the Mn within the chalcopyrite lattice. Type E and Type F reflections both have the same structure factor values as shown in the equations below.

Type D $\Rightarrow$ h and k, one odd, one even, l is odd

$$\mathcal{F}^2 = 4(f_{Ag/Cu} - f_{Ga})^2$$

Type E $\Rightarrow$ h and k even, l singly even

$$\mathcal{F}^2 = 16[z(f_{Ag/Cu} + f_{Ga} - 2f_{Mn})]^2$$

Type F $\Rightarrow$ h and k odd, l doubly even

$$\mathcal{F}^2 = 16[z(f_{Ag/Cu} + f_{Ga} - 2f_{Mn})]^2$$

The variation of the structure factors for differing concentrations of manganese in both systems, for the stannite ordered arrangement, are shown in Figure 13.

Since the structure factor is proportional to the intensity of the reflected beam, the ratio of structure factors of different postulated Mn-ordered structures with experimental Bragg peak intensities will be found. The additional Bragg peaks that appear in the stannite type of ordered arrangement (Type E and Type F) will also be looked for in the diffraction spectra of both systems at specific manganese concentrations.

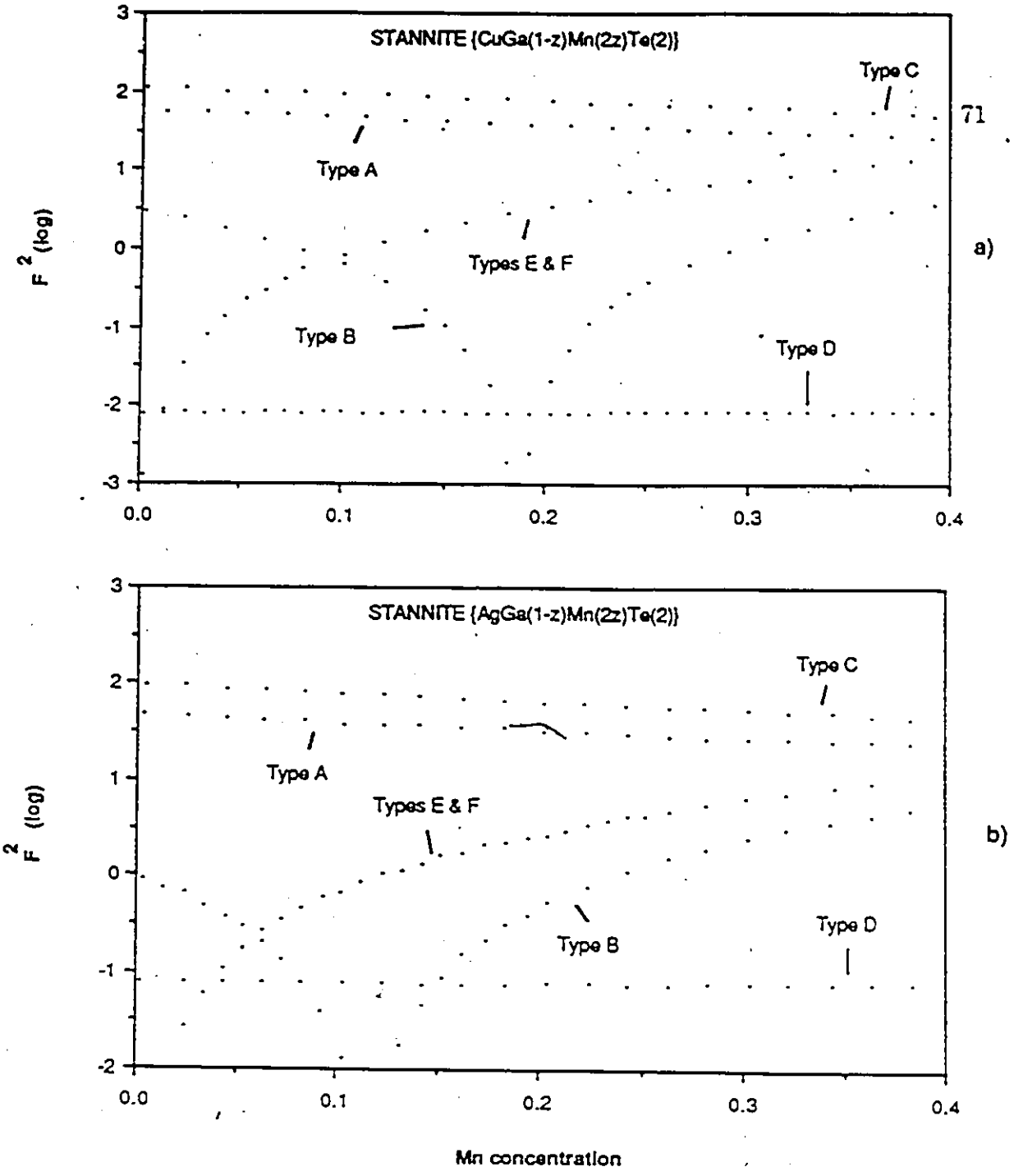

Figure 13: Variation of structure factors with manganese concentration z for the stannite ordered arrangement of the a) $(CuGa)_{1-z}Mn_{2z}Te_2$ and b) $(AgGa)_{1-z}Mn_{2z}Te_2$ systems.

4.5 Results and Analysis

Each "well defined" Bragg peak, in both neutron diffraction spectra obtained, were fitted to a Gaussian distribution and the appropriate FWHM and Bragg angle were recorded. The "integrated intensity" of each one of these peaks, where possible, was calculated.

The structure factors for the reflections of the proposed Mn-ordered structures were calculated and their ratios with the experimental intensities tabulated. Because of the proportionality between intensity and the structure factor, these ratios should produce a constant value for any reflection if the particular ordered structure is truly observed. The experimental positions of the Bragg peaks for the proposed ordered structures were also found and compared to the experimental results.

4.5.1 $(CuGa)_{1-z}Mn_{2z}Te_2$ system with $z = 0.2$

As had been discussed earlier, the $z = 0.2$ sample for this system clearly shows two phases from the neutron diffraction measurements, chalcopyrite and $MnTe$. This confirms the results obtained in the T(z) diagram (Figure 3 in Chapter 2) that the equilibrium condition at $T = 200°$ C and $z = 0.2$ is two phase. For this reason, any analysis related to the ordering of the manganese in this system was discontinued.

From the neutron spectrum obtained for this system as shown in Figure 14, and using the lattice parameters obtained from the (400) and (008) Bragg peak positions on the diffraction spectrum, we found that the Bragg peaks labelled 1 to 11 correspond to the structure reflections (Type A, B and C). Using the calculated chalcopyrite structure factors, the intensity of the "well resolved" peaks (3, 4, 8 and

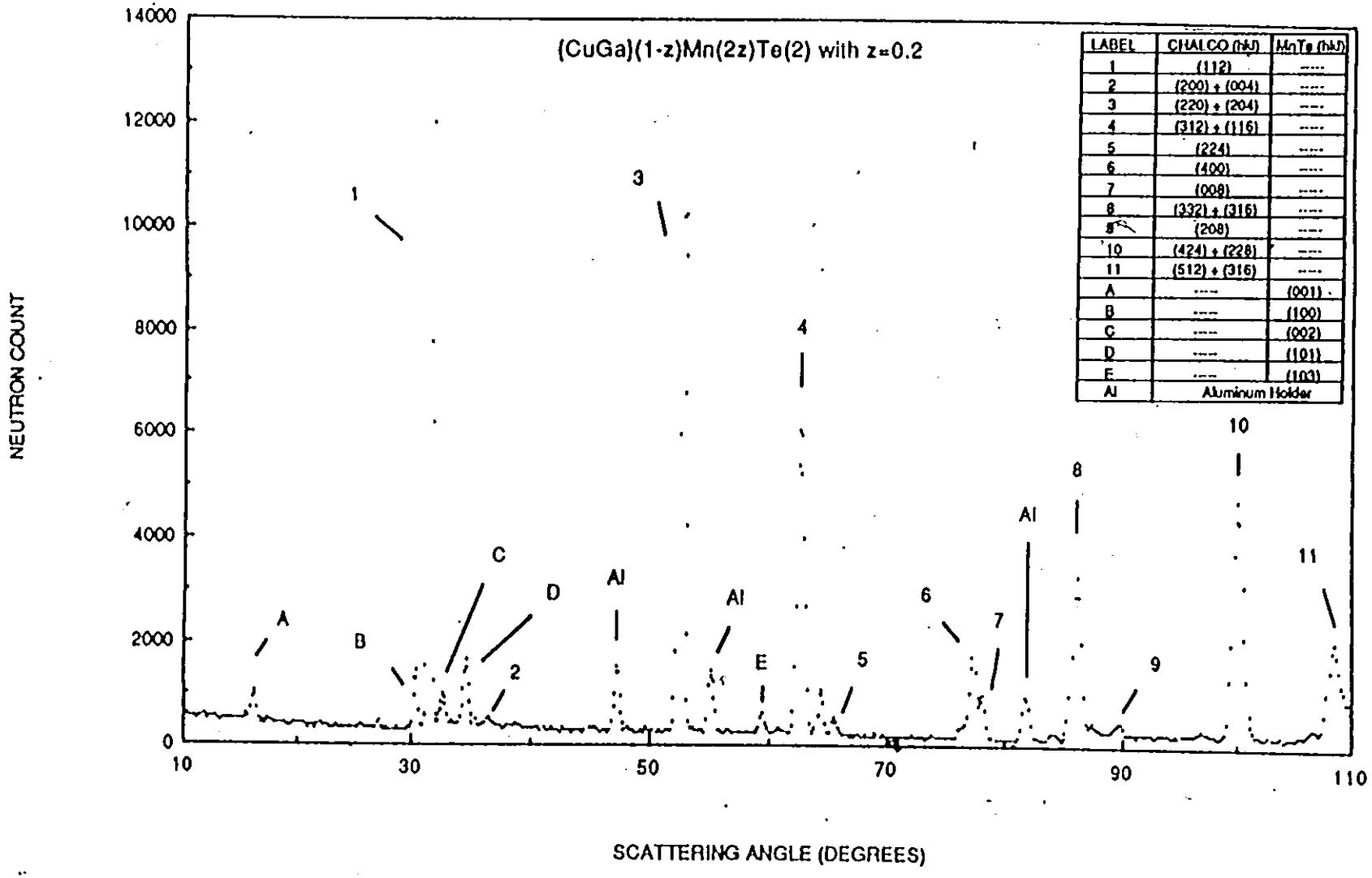

Figure 14: Neutron diffraction spectrum for a $(CuGa)_{1-z}Mn_{2z}Te_2$ sample of $z = 0.2$ composition annealed at 300° C.

10) were found to fit very well with the calculated intensities for these Bragg peaks expected in the chalcopyrite structure. The other Bragg peaks for the chalcopyrite phase could not be analyzed using intensity considerations due to bad resolution, but, by comparing the experimental Bragg peak positions with those expected for this case, all observable peaks were in agreement. The values of the lattice parameters obtained from the diffraction spectrum showed the same composition of the chalcopyrite phase as that obtained when finding the two phase region boundary for the equilibrium diagram of this system in Chapter 2.

By calculating the Bragg peak positions for $MnTe$ using its tabulated hexagonal cell lattice parameters of $a = 4.1429\text{Å}$ and $c = 6.7073\text{Å}$, they were found to correspond exactly with the second phase's experimental Bragg peak positions on this particular diffraction spectrum.

4.5.2 $(AgGa)_{1-z}Mn_{2z}Te_2$ system with $z = 0.4$

From the neutron diffraction spectrum of a $z = 0.4$ sample for this system, Figure 15, we can see that the larger peaks seem to have that distinct chalcopyrite feature where line splitting increases as Bragg angle increases. The Bragg peaks numbered 1 to 6 and 8 to 15 correspond to the expected Bragg peak positions of the Type A, B and C reflections of the chalcopyrite structure using its experimental lattice parameters [1]. This is shown in Table 3.

Relative intensity problems between Bragg peaks of the same type and intensity disagreements between calculated and experimental Bragg peaks of all types were encountered and will be discussed in more detail later.

Now we can look for any indication of the proposed Mn-ordered structures.

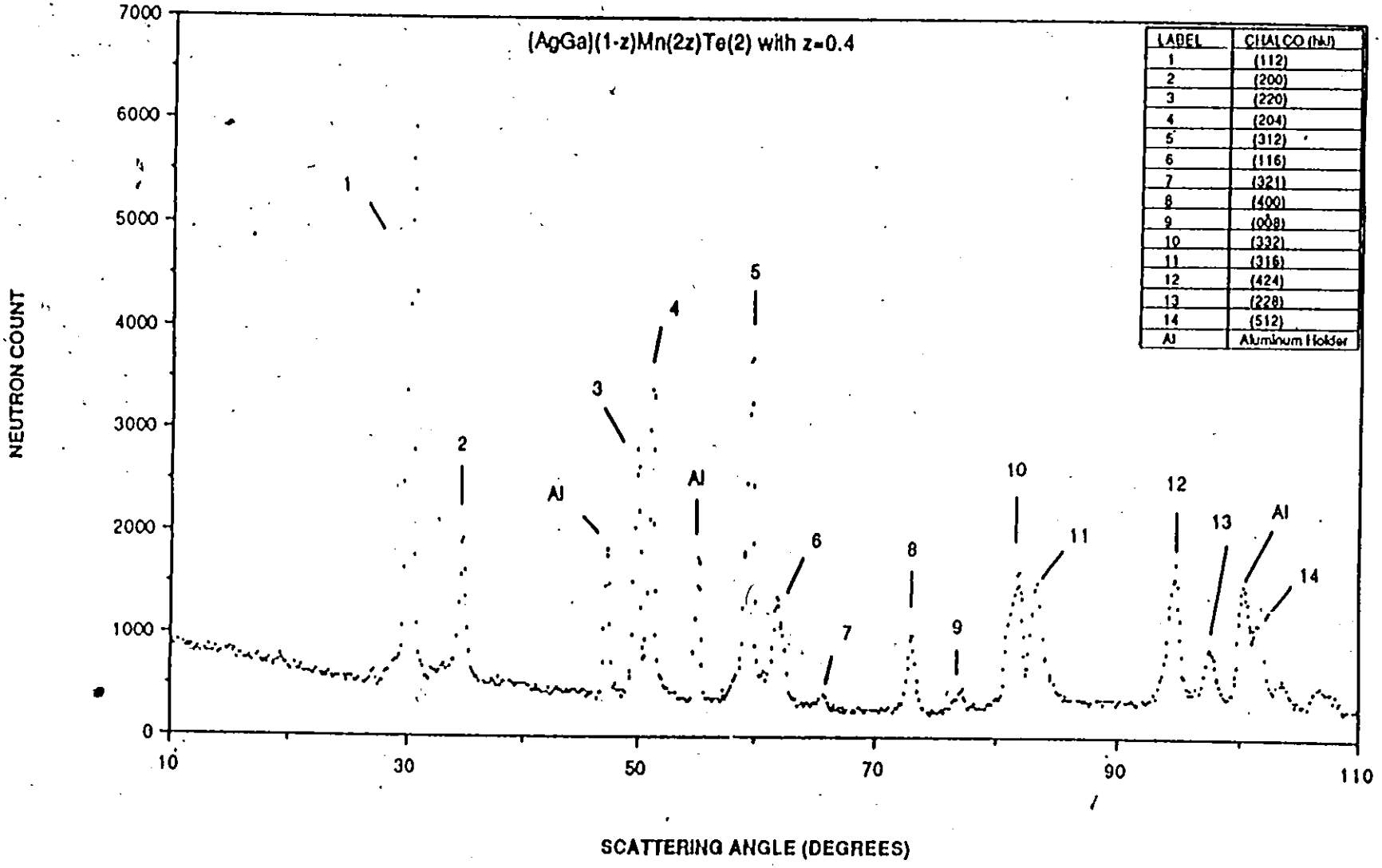

Figure 15: Neutron diffraction spectrum for the $(AgGa)_{1-z}Mn_{2z}Te_2$ system with $z = 0.4$ sample annealed at 200° C.

Peak #	Type	(hkl) plane	Calculated Pos'n (°)	Experimental Pos'n (°)
1	A	(112)	30.32	30.26
2	B	(200)	34.53	34.73
3	C	(220)	49.63	49.82
4	C	(204)	51.04	51.02
5	A	(312)	59.28	59.35
6	A	(116)	61.79	61.65
7	D	(321)	65.60	65.61
8	C	(400)	72.82	73.00
9	C	(008)	77.33	76.98
10	A	(332)	80.87	81.00
11	A	(316)	83.08	83.20
12	C	(424)	94.35	94.43
13	C	(228)	97.63	97.49
14	A	(512)	101.17	101.35
15	A	(336)	103.39	103.30

Table 3: Table showing the experimental and calculated positions of the Bragg peaks for the chalcopyrite structure of the $(AgGa)_{1-z}Mn_{2z}Te_2$ sample with $z = 0.4$ composition.

For the case where the Mn orders at random on the Ag or Ga sublattices, the structure factor equation for the Type D reflections give values of $\mathcal{F}^2$ of 5.84 and 5.11, respectively, for this composition as shown in Figure 12(b). Since these values are almost equal to that of the Type B reflections, and if this ordering scheme is to be observed, we can expect Bragg peaks at the appropriate positions on the spectrum that have just about the same intensity as the Type B peaks. We can see from the neutron diffraction spectrum for this system, Figure 15, that Bragg peak #7, which is a Type D reflection, does not have an intensity even closely resembling that of a Type B reflection (Bragg peak #2). From this observation, we can say that the Mn does not order at random on the Ag or Ga sublattices in the Mn-ordered chalcopyrite state.

For the proposed stannite type of Mn-ordered arrangement, the $\mathcal{F}^2$ values for the Type D reflections is 0.075 and that of the Types E and F reflections is 10.97 (earlier we showed that Type E and F reflections have the same structure factor values) as shown in Figure 13(b).

We must be careful when trying to identify the Type D reflections for the stannite like arrangement. The reasoning behind this is that the Type D reflections for the chalcopyrite structure case will be positioned at exactly the same Bragg angle and its' $\mathcal{F}^2$ value, being 0.15, is the same order of magnitude as the above mentioned one. Trying to categorize the peak (i. e. deciding whether the Bragg reflection is due to the chalcopyrite arrangement or the stannite type arrangement) solely on intensity considerations is not sufficient. Thus, we are left with the identification of any Type E and F reflection Bragg peaks to uphold the proposed stannite like Mn-ordered structure.

Since the Type E and F reflections' $\mathcal{F}^2$ value is an order of magnitude greater than that of the Type B reflections, the presence of the former reflections' Bragg peaks should be quite clear in the spectrum. With careful calculation of the expected positions of the Type E and F Bragg peaks, we see from the diffraction pattern, Figure 15, that no such peaks occur using the present sample. As an example, there would be peaks at $2\theta = 53.21°$ and $2\theta = 77.97°$ corresponding to the (222) and (226) reflection planes respectively, but, no such reflections are observed.

Therefore, the proposed stannite like Mn-ordering arrangement does not occur in the present sample.

As was mentioned earlier, intensity disagreement was also observed in the Type A, B and C reflection Bragg peaks. This can be seen on the diagram of Figure 16, made by Dr. David Noakes at the Chalk River Nuclear Labs, using a Rietveld fit analysis of the neutron diffraction data for a chalcopyrite structure of this sample. The full line represents the calculated expected spectrum for this sample having the chalcopyrite structure. The dotted line represents the actual data obtained. From this figure we can see that the intensity of some experimental Bragg peaks (labelled 1, 2, 3, 5, 8, 10, 11, 12 and 14) is always larger than that tabulated for pure chalcopyrite.

By trying to adjust the intensity of the calculated Bragg peaks by some constant factor, the correlation between both plotted spectra became even worse. Because of the positions of the intensity errant experimental peaks, it was suggested by Dr. Noakes and Dr. Holden to include the contribution of a cubic phase to that of the chalcopyrite phase. Because no Rietveld fit programm being able to combine two

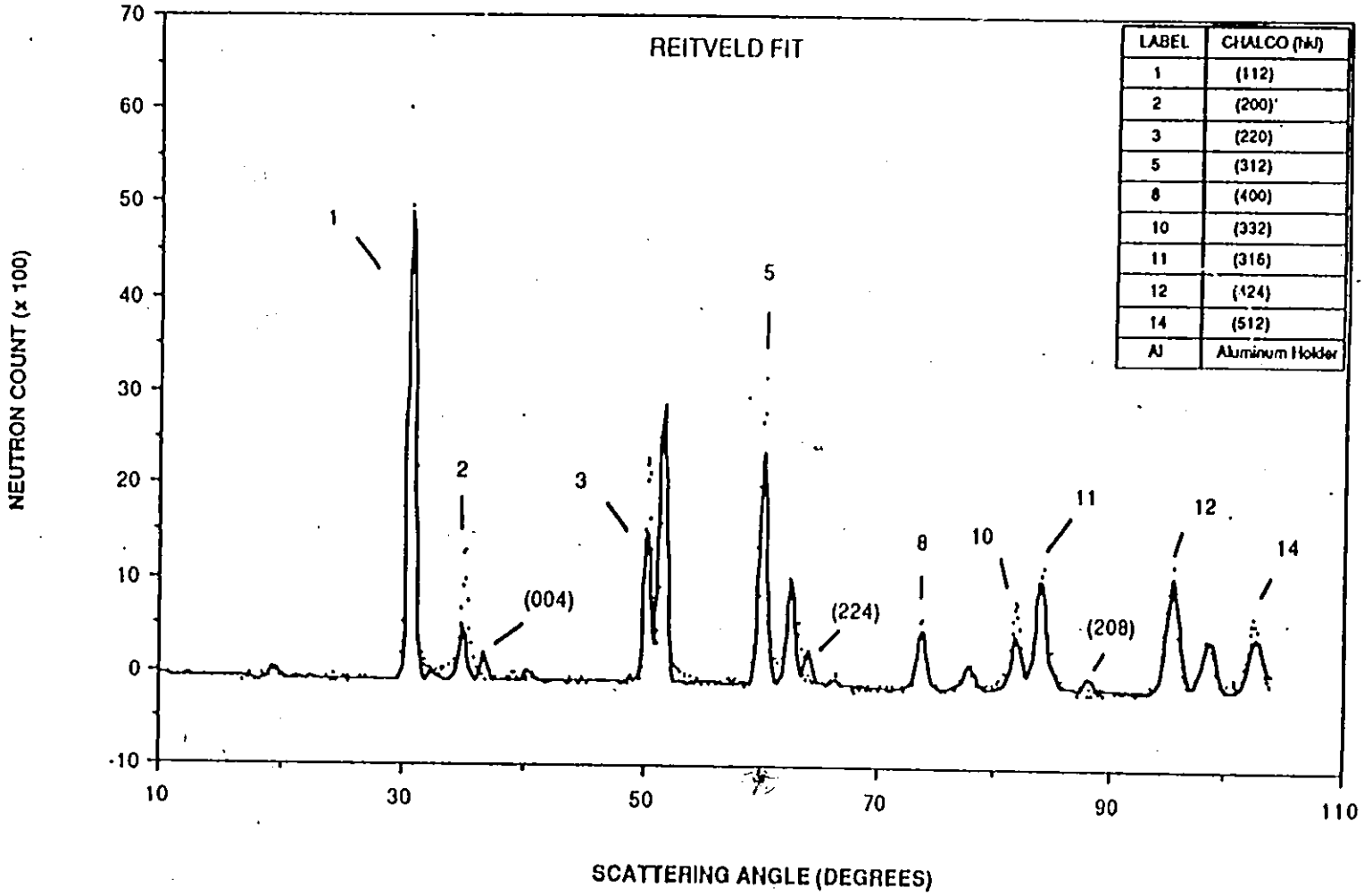

Figure 16: Rietveld fit of chalcopyrite structure for the $(AgGa)_{1-z}Mn_{2z}Te_2$ system with $z = 0.4$ where full line is the calculated spectrum and dotted line is experimentally observed spectrum.

phases was available, a modelling of the cubic structure factors as merely the chalcopyrite ones for c/a=2.0 was used. Estimates of the cubic Bragg peak intensities superimposed to the chalcopyrite peak intensities gave very good correlation between the observed and calculated intensity ratios for the above mentioned Bragg peaks.

This $z = 0.4$ sample of the $(AgGa)_{1-z}Mn_{2z}Te_2$ system is thus a mixture of the chalcopyrite and cubic zinc-blende phases. No apparent ordering of the types proposed was observed during this analysis because of the annealing and quenching conditions used to prepare this sample.

One interesting aspect of the diffraction spectrum for this sample is that the reflections occuring on (hkl) planes where $l^2 > h^2 + k^2$ seemed to have their Bragg peak intensities suppressed. This can be seen from Figure 16 where the reflections from planes (004), (224) and (208) should occur with intensities matching those of Bragg peak #2 .

From ESR data, it was suggested by Dr. Woolley that an Mn-ordering of the type where the Mn totally fills certain planes perpendicular to the c axis in the chalcopyrite structure could be occuring. Depending on the manganese concentration, only a certain number of planes could be totally filled over a number of 'c' axis lattice lengths. This increased c lattice parameter in this ordered structure would alter the reflections along the c axis direction thereby reducing the intensity of any reflection involving a large 'l' Miller indice. This will be discussed in more detail in the conclusion and discussion.

4.6 Conclusion and Discussion

From the neutron diffraction results and analysis of the $(CuGa)_{1-z}Mn_{2z}Te_2$ system with $z = 0.2$ composition annealed at 300° C, we see that it had a two phase structure, chalcopyrite and $MnTe$. Initial measurements of magnetic susceptibility and ESR on this sample had indicated that an ordered structure was present. It is clear that the ordered form that was initially observed represented higher temperature phases which were retained at room temperature as a result of quenching conditions and which were lost after the annealing period at lower temperatures. This sample probably doesn't show any type of Mn-ordering in an equilibrium state. Even though the present results do not include anything pertinent to the ordering state of this sample, they do in fact support the results mentioned earlier in Chapter 2 for the T(z) diagram, Figure 3, that had only been made available after the present diffraction work, indicating the two phase equilibrium condition at T= 300° C for the $z = 0.2$ composition in this system.

In the case of the sample of the $(AgGa)_{1-z}Mn_{2z}Te_2$ system with $z = 0.4$ composition annealed at 200° C, it was found that two phases are present, chalcopyrite and cubic zinc-blende. This can also be explained when considering this system's T(z) diagram, Figure 4 in Chapter 2. This sample had initially been annealed at 600° C, within the cubic phase region, and then quickly quenched. A second annealing period at 200° C was performed within the Mn-ordered region. The first annealing period and subsequent quenching certainly produced a sample in which some cubic structure was retained. This phase was not completely lost after the second annealing period at a lower temperature. It is probable that at 200° C the

diffusion rates are too small and so little crystallographic change can occur. Thus, it is obvious that a different heat treatment is necessary to observe any Mn-ordered structure.

This sample also did not show any Mn-ordering of the type proposed because of an annealing temperature that was too low but did in fact exhibit a curious behavior with regards to the intensity of the reflections from planes having high l Miller indices. As was mentioned earlier, this could be expected if the Mn entered totally into some (001) planes of the chalcopyrite lattice, giving another type of Mn-ordered structure. Work presently being done by Riccardo Brun del Re [4] for his Ph. D. thesis at the University of Ottawa seems to indicate that, in this system, a different type of Mn-ordering is occuring at temperatures of 200° C and below. His magnetic susceptibility measurements show signs of planar Mn-ordering at these temperatures. The behavior observed in the present sample would tend to support this .

The proposed types of Mn-ordering presented earlier (stannite-like) cannot be excluded because of the annealing temperatures and quenching conditions used to produce the present $(AgGa)_{1-z}Mn_{2z}Te_2$ sample. These types of ordering arrangements and the planar type of ordering mentioned above will be investigated further using neutron diffraction by another member of the group at the University of Ottawa [4].

Chapter 5

Conclusion

An investigation into the proposed types of crystallographic ordering arrangements of manganese within the chalcopyrite lattices of the separate binary alloy systems $(CuGa)_{1-z}Mn_{2z}Te_2$ and $(AgGa)_{1-z}Mn_{2z}Te_2$ has been presented. The main types of measurements that were pertinent to this work were lattice parameter determination, magnetic susceptibility, ESR linewidth and neutron diffraction.

In Chapter 2, it was shown that the $(CuGa)_{1-z}Mn_{2z}Te_2$ system has a very narrow single phase solubility range of about $0 \leq z \leq 0.04$ at $\sim 200°$ C. From the phase diagram, Figure 3, that had been made available only after the present work, it was found that no Mn-ordered zinc-blende or Mn-ordered chalcopyrite phases exist in the equilibrium diagram, though it appears that rapidly quenched samples retain "metastable" phases in different proportions according to quenching conditions.

The phase diagram, Figure 4, combined with preparatory x-ray work show that the $(AgGa)_{1-z}Mn_{2z}Te_2$ system has a wide range of solid solution ($0 \leq z \leq 0.55$)

with Mn-ordering occuring in both zinc-blende and chalcopyrite structures in the 300° C - 400° C temperature range.

The results from Chapter 3 indicate that ordering of the manganese ions on the cation sublattices occurs in these alloys at lower temperatures, in agreement with [24]. ESR measurements made on the $(CuGa)_{1-z}Mn_{2z}Te_2$ sample with $z = 0.2$ that had been quenched from 650° C to room temperature showed very narrow linewidths indicating an Mn-ordered arrangement. This ordered state, also initially observed in magnetic susceptibility measurements [12], was shown to represent a high temperature "metastable" phase which was still present after cooling from 650° C. This phase was lost after annealing for a long period at 300° C, in preparation for neutron diffraction, resulting in a two phase equilibrium condition.

We also notice that the $(AgGa)_{1-z}Mn_{2z}Te_2$ system is very sensitive to annealing and quenching conditions. We found from ESR and magnetic susceptibility data that the sample of $z = 0.4$ from this system, quenched rapidly from higher temperatures down to room temperature, produced a sample that retained some of the high temperature phases. A sample quenched slowly in air down to room temperature retained less of the high temperature phases and more of the low temperature phase. A similar sample annealed at 200° C initially showed the presence of the Mn-ordered chalcopyrite structure from magnetic results but neutron diffraction measurements later indicated that a little of the high temperature cubic phase was still retained. The possible Mn-ordered arrangement observed was not of the preferred cation sublattice type nor the stannite-like type but likely to be a planar-type of ordering.

Chapter 4 dealt with the neutron diffraction measurements on the $z = 0.2$

$(CuGa)_{1-z}Mn_{2z}Te_2$ sample annealed at 300° C and the $z = 0.4$ $(AgGa)_{1-z}Mn_{2z}Te_2$ sample annealed at 200° C. Structure factors for all the proposed Mn-ordered structures were calculated and used in a comparison procedure between observed intensity and calculated intensity of most Bragg peaks obtained. Both systems showed the characteristic gradual Bragg peak separation common to the chalcopyrite structure as the scattering angle is increased.

The $z = 0.2$ $(CuGa)_{1-z}Mn_{2z}Te_2$ sample was found to be of a two phase structure, chalcopyrite and $MnTe$, and thus did not contain any Mn-ordered structure. The presence of an ordered structure in this sample after having been quenched from 650° C down to room temperature, as shown in previous magnetic measurements, was probably a result of quenching conditions that introduced "metastable" phases which were lost after an annealing period at 300° C. Because of the narrow range of single phase solubility in this system (Figure 3 in Chapter 2), this system probably does not show any Mn-ordering in its equilibrium state.

The $(AgGa)_{1-z}Mn_{2z}Te_2$ sample of $z = 0.4$ composition that had been annealed at 200° C was found to be, through neutron diffraction measurements, a mixture of two phases, chalcopyrite and cubic. This is consistent with the equilibrium diagram (Figure 4 in Chapter 2) when you consider that the first annealing period at 600° C and subsequent quenching had caused the sample to retain a little of the cubic phase down to room tempetature. The second annealing period at 200° C did not completely get rid of this cubic phase. This is also consistent with the magnetic measurements made on this sample. At 200° C, the diffusion rates are too small to greatly affect the crystallographic structure. Thus, different heat treatment is obviously necessary to encourage the Mn-ordering process. Because of the too low

annealing temperature, this sample did not show any signs of Mn-ordering of the preferred cation sublattice type or the stannite-like type. The observed intensities of the Type D Bragg peaks did not correlate with any of the calculated intensities for these reflections for the case where the manganese enters one cation sublattice at random. Also, the Type E and F reflections that occur in the calculated stannite-like ordering arrangement did not appear in this sample's diffraction spectrum (Figure 15 in Chapter 4). There was in fact the absence of Bragg peaks for reflections occuring on the (hkl) planes that had $l^2 > h^2 + k^2$. This interesting behavior could be the result of the manganese entering totally into some (001) planes of the chalcopyrite lattice, showing another type of Mn-ordered structure.

By comparing the above mentioned planar Mn-ordering with other work presently being done on this system [4], the results seem to indicate that this second type of Mn-ordering (planar-type) exists at temperatures below 200° C. In light of these results, we cannot exclude the stannite-like type of Mn-ordering because of the chosen annealing temperatures and quenching conditions used to produce the present $(AgGa)_{1-z}Mn_{2z}Te_2$ sample.

It is clear that this investigation into the Mn-ordering in the $(CuGa)_{1-z}Mn_{2z}Te_2$ and $(AgGa)_{1-z}Mn_{2z}Te_2$ systems presented in this thesis has yielded important information regarding the types of Mn-ordering arrangements within these materials and also showed the major role that heat treatment takes on when studying such systems. The investigation of the Mn-ordering in the $(AgGa)_{1-z}Mn_{2z}Te_2$ system will keep going through the work of Riccardo Brun del Re as part of his Ph. D. research at the University of Ottawa. Better heat treatments in producing the samples are now being used with heavy emphasis on obtaining a sample that possesses

a planar-type of Mn-ordered structure. The work presented here along with the present work being done is part of an ongoing program for this group at the University of Ottawa to study and better understand a wide range of semimagnetic semiconductor systems.

Bibliography

[1] M. Al-Najjar. Master's thesis, University of Ottawa, 1986.

[2] A. Aresti, L. Garbato, A. Geddo Lehman, and P. Manca. *Mat. Res. Soc. (International Conference on Ternary and Multinary Compounds*, 497, 1987.

[3] N.B. Brandt and V.V. Moshchalkov. *Advances in Physics*, 33, 1984.

[4] R. Brun del Re. Work towards a Ph.D. Thesis.

[5] S. Chehab. PhD thesis, University of Ottawa, 1986.

[6] B. Coles. *Amorphous Magnetism.* 1973.

[7] H. Dachs. *Neutron Diffraction.* Springer-Verlag, 1978.

[8] T. Donofrio. PhD thesis, University of Ottawa, 1986.

[9] J.K. Furdyna. *Journal of Applied Physics*, 53, 1982.

[10] G. Gagliotti, A. Poaletti, and F.P. Ricci. *Nucl. Instr. Meth.*, 3:223–228, 1958.

[11] J.A. Gaj. *J. Phys. Soc. Japan (Proceedings of the 15th International Conference on Physics of Semiconductors, Kyoto (1980))*, 49 suppl. A, 1980.

[12] R. Goudreault. Master's thesis, University of Ottawa, 1987.

[13] C.N. Guy. *Physica B*, 86-88:877–879, 1977.

[14] A.P. Murani. *Physical Review Letters*, 37:450–453, 1976.

[15] C. Neal. Master's thesis, University of Ottawa, 1987.

[16] M. Quintero. PhD thesis, University of Ottawa, 1984.

[17] M. Quintero, P. Grima, R. Tovar, G.S. Perez, and J.C. Woolley. 1988- accepted by Phys. Stat. Sol.

[18] M. Quintero, R. Tovar, M. Al-Najjar, G. Lamarche, and J.C. Woolley. 1988- Accepted by J. Sol. State Chem.

[19] G. Toulouse. *Comm. Phys.*, 2:115–119, 1977.

[20] H. Watanabe. *Progress of Theoretical Physics*, 18(4):405–420, 1957.

[21] J.E. Wertzand and J.R. Bolton. *Electron Spin Resonance, Elementary Theory and Practical Applications*. McGraw-Hill, 1972.

[22] B.T.M. Willis (ed.). *Thermal Neutron Diffraction (Proceedings of the International Summer School at Harwell, 1-5 July (1968), on the Accurate Determination of Neutron Intensities and Structure Factors)*. Oxford University Press, 1970.

[23] J.C. Woolley. *Compound Semiconductors I*, page p.3. Reinhold, 1962.

[24] J.C. Woolley, G. Lamarche, A. Manoogian, M. Quintero, L. Dierker, M. Al-Najjar, D. Proulx, C. Neal, and R. Goudreault. *Mat. Res. Soc. (Proceedings of the 7th International Conference on Ternary and Multinary Compounds, Colorado (1986))*, 1987.